Tunable Phase Junctions in Bi_2O_3–$BiVO_4$ Thin Films via Reactive Magnetron Co-Sputtering for Efficient Carrier Separation and Enhanced Photoelectrochemical Performance

Tayebeh Sharifi[a,*], Krešimir Salamon[b], Tecush Mohammadi[c], Dražan Jozić[d], Robert Peter[e], Bor Arah[f], Aleš Lapanje[a], Marko Štrok [a,**]

[a] Jožef Stefan Institute, Jamova cesta 39, 1000 Ljubljana, Slovenia

[b] Rudjer Bosković Institute, Bijenička cesta 54, 10000 Zagreb, Croatia

[c] National Institute of Chemistry, Hajdrihova 19, 1000 Ljubljana, Slovenia

[d] Faculty of Chemistry and Technology, University of Split, Ruđera Boškovića 35, 21000 Split, Croatia

[e] University of Rijeka, Faculty of Physics and Centre for Micro- and Nanosciences and Technologies, Radmile Matejčić 2, 51000 Rijeka, Croatia

[f] Center for Electron Microscopy and Microanalysis, Jožef Stefan Institute, Jamova cesta 39, 1000 Ljubljana, Slovenia

To whom correspondence should be addressed:

e-mails: tayebeh.sharifi@ijs.si (*), marko.strok@ijs.si (**)

Preprint not peer reviewed

This preprint research paper has not been peer reviewed. Electronic copy available at: https://ssrn.com/abstract=5365557

Abstract:
Engineering efficient photoelectrode materials requires precise control of the structural, optical, and interface properties of thin semiconductor films. In this work, reactive magnetron co-sputtering (RMS) was used to fabricate Bi-based thin films with tailored phase compositions, focusing on the relationship between the phase structure and the photogenerated charge transport behavior. By fine-tuning the sputtering parameters, specifically the Bi/V target power ratio and annealing temperature, films comprising Bi_2O_3–dominant phase, a pure $BiVO_4$ phase and well-defined Bi_2O_3–$BiVO_4$ p–n heterojunctions were synthesized, as confirmed by X-ray diffraction and X-ray photoelectron spectroscopy. High-temperature Grazing Incidence X-ray Diffraction revealed temperature-induced phase transitions, with Bi_2O_3 being stable at lower temperatures and $BiVO_4$ crystallizing above ~400 °C. Photoelectrochemical characterization demonstrated that Bi_2O_3–$BiVO_4$ heterojunction thin films (BO/BVOs) significantly outperform their phase–dominant $BiVO_4$ and Bi_2O_3 counterparts when synthesized at optimal phase compositions. This performance enhancement is attributed to efficient charge separation driven by internal electric fields at the p–n interface. In particular, the optimized BO/BVO–1 film exhibited a photocurrent density more than 2.5 times higher than that of pure $BiVO_4$ at 1.23 V vs. RHE, and over 9 times higher at 1.63 V vs. RHE. Electrochemical impedance spectroscopy analysis revealed suppressed surface recombination and enhanced charge transfer at the interface in the heterojunction samples, highlighting the role of nanoscale junctions in boosting photoelectrochemical performance. These findings indicate that scalable methods like RMS can enable precise phase engineering and heterojunction design for efficient solar photoanodes.

Keywords: Magnetron co sputtering, Bi_2O_3, $BiVO_4$, p–n hetrojunction, High-temperature Grazing Incidence X-ray Diffraction (HT-GIXRD)

Preprint not peer reviewed

This preprint research paper has not been peer reviewed. Electronic copy available at: https://ssrn.com/abstract=5365557

1. Introduction

The development of efficient materials for photocatalytic and photoelectrochemical (PEC) application is crucial for addressing current energy and environmental challenges through solar-driven processes. In particular, narrow band gap semiconductors show great potential for visible-light-driven applications such as water splitting, water treatment or degradation of organic pollutants. Bismuth (Bi)-based semiconductors have emerged as attractive photocatalysts due to their favorable band structures, low toxicity, and ease of synthesis, with bismuth vanadate ($BiVO_4$) being among the most promising candidates [1, 2]. However, its performance is significantly limited by high recombination rates of photogenerated charge carriers both within the bulk of the semiconductor and at the semiconductor–electrolyte interface (SEI), where sluggish charge transfer kinetics further limit efficiency [3, 4].

To address these limitations, extensive efforts have focused on modifying $BiVO_4$ through various strategies, including metal and non-metal doping, surface functionalization, and the formation of homo/heterojunctions [4, 5]. Among these, constructing heterojunctions, especially type-II or p–n junctions, has proven highly effective in enhancing charge separation [6, 7]. At the interface between two semiconductors with suitable band alignments, an internal electric field can be formed that promotes the seperation of electrons (e^-) and holes (h^+) and suppresses their recombination. The construction of heterojunctions has been extensively investigated with different semiconductors and enhanced photocatalytic activity has been reported due to improved photogenerated charge carrier lifetime and mobility, that is, due to the suppressed recombination and better charge separation efficiency [8, 9].

In particular, Bi_2O_3–$BiVO_4$ heterojunctions have exhibited superior photocatalytic performance compared to single-phase Bi_2O_3 or $BiVO_4$. This enhancement is largely due to their complementary optoelectronic properties and favorable band alignment, which improve visible-light absorption and charge separation efficiency [6, 10-14]. However, the actual degree of improvement remains a subject of debate. This uncertainty arises largely from variations in crystalline quality, morphology, surface area, and other synthesis-dependent factors. The optimization of these parameters is crucial, as they significantly affect the overall efficiency of photocatalysis. In particular, precise control of the crystalline phase and morphology can have a significant impact on performance.

To date, Bi_2O_3–$BiVO_4$ heterojunctions have been synthesized predominantly by wet-chemical methods, including hydrothermal synthesis, sol–gel processing, and co-precipitation [6, 15-17]. While these methods offer compositional flexibility, they often have issues with phase purity, reproducibility, and difficulties in scaling up for device integration. Moreover, these methods typically yield Bi_2O_3–$BiVO_4$ powders, which require additional steps for catalyst recovery and immobilization onto conductive substrates, factors that hinder practical PEC applications.

In contrast, in situ thin film growth on conductive substrates provides a more practical and scalable solution, simplifying device integration and enhancing performance in PEC systems. Physical vapour deposition techniques such as sputtering offer a highly controlled and scalable route for the production of thin film photocatalysts. Among them, magnetron

This preprint research paper has not been peer reviewed. Electronic copy available at: https://ssrn.com/abstract=5365557

co-sputtering offers several key advantages, including the use of pure metal targets instead of chemical precursors, precise control of film thickness and composition, high purity, and compatibility with device fabrication processes [4, 18-20]. Given the growing interest in Bi–based materials, it is important to understand how the fabrication of Bi–based thin films using sputtering techniques affects their structural and functional properties in order to optimize their performance in photocatalytic and PEC applications.

Although several studies have reported the fabrication of pure phase $BiVO_4$ [4, 21, 22] and Bi_2O_3 [23-25] thin films via sputtering, to the best of our knowledge, no previous work has reported the fabrication of tunable phase junction Bi_2O_3–$BiVO_4$ thin films using RMS as a strategy for interface engineering in photoelectrodes.

In this study, a series of thin films were fabricated via reactive magnetron co-sputtering (RMS) using Bi and vanadium (V) metal targets in the presence of oxygen as a reactive gas. By tuning the RMS parameters, including target power, oxygen partial pressure and post-deposition annealing temperature, we successfully controlled the phase composition of the films, ranging from Bi_2O_3-dominant, over the Bi_2O_3–$BiVO_4$ phase composition to the pure $BiVO_4$ phase. The structural, morphological, and compositional properties of the thin films were investigated using various techniques, particularly high-temperature Grazing Incidence X-ray Diffraction (HT-GIXRD), scanning electron microscopy (SEM), and X-ray photoelectron spectroscopy (XPS). The PEC performance of the films was systematically evaluated under both light illumination and dark conditions. Our results demonstrate that RMS, as a scalable technique, is a promising approach for engineering high-performance Bi-based photocatalytic thin films with tunable properties for solar energy conversion.

2. Experimental

2.1 Magnetron co-sputtering thin films fabrication

Bismuth–based thin films were fabricated using a magnetron sputtering system (Elettrorava model ER-SM500), equipped with metallic Bi and V targets (7.62 cm diameter, 99.99 at.% purity), each tilted at 15° relative to the vertical axis. The targets were powered independently using direct current (DC) supplies, allowing precise control of the deposition rate of each metal and therefore the composition of the film. The films were grown with reactive oxygen gas supplied near the substrate with partial pressure of O_2 controled by MKS mass flow controller in the range 0-6 (standard cubic centimeters per minute (sccm)) [26]. The flow of Ar sputtering gas was adjusted at 25 sccm (equivalent to 4 mTorr partial pressure) and kept constant for all depositions. A series of Bi_2O_3–$BiVO_4$ thin films were fabricated by systematically varying the Bi and V power (deposition rate) and the O_2 partial pressures (**Table S1** and **Figure S1**). Given the significantly higher sputtering yield of Bi compared to V, the DC power for the V target was adjusted in the range of 250-300 W, while the Bi target power was varied between 12 and 19 W to tune the V/Bi atomic ratio, which is crucial for optimizing the formation of the Bi_2O_3 –dominant and pure $BiVO_4$ phases, and their mixture.

All films were deposited at room temperature onto glass substrates (~1 × 1.5 cm^2) coated with fluorine-doped tin oxide (FTO). Before deposition, the substrates were cleaned

This preprint research paper has not been peer reviewed. Electronic copy available at: https://ssrn.com/abstract=5365557

by sequential ultrasonication in isopropanol, acetone, and deionized water for 15 minutes each, then dried under a nitrogen stream. The substrates were mounted perpendicular to the vertical axis at a distance of ~15 cm from the targets and rotated during deposition to ensure uniform film growth. The deposition time was adjusted to achieve a final film thickness of approximately 150 nm.

X-ray diffraction (XRD) was used to identify the resulting phases and optimize RMS parameters for their formation (**Table S1**). Since the as-deposited films were amorphous, all samples were annealed in air at 400 °C for one hour to induce crystallization. This thermal treatment enabled the formation of dominant distinct phases, including Bi_2O_3, $BiVO_4$, and Bi_2O_3–$BiVO_4$ phase composition.

2.2 Material characterization

Film thickness, uniformity, and surface roughness were assessed using X-ray reflectivity (XRR) measurements. Preliminary phase identification was performed through grazing incidence X-ray diffraction (GIXRD) at a fixed incidence angle of 0.9° relative to the sample surface. Both XRR and GIXRD analyses were conducted using a Siemens D5000 diffractometer equipped with a copper anode, operated at 40 kV and 40 mA, and Goebel mirror and a graphite monochromator for X-ray beam shaping. In–situ high-temperature Grazing Incidence X-ray Diffraction (HT-GIXRD) analysis was also performed on selected samples using an Empyrean X-ray diffraction system (Malvern PANalytical, UK) equipped with an HTK 1200N high-temperature chamber (Anton Paar, Austria) at the sample holder position. The system used a copper X-ray tube (λKα1=1.5406 Å), iCore/dCore multicore optics, and a PIXcel3D detector. For HT-GIXRD measurements, films were prepared on silicon substrates and heated in the high-temperature chamber in an air atmosphere in a temperature range from 50 °C to 700 °C in 10 °C steps, with a heating rate of 10 °C/min and a 10-minute thermal equilibration prior to sample alignment and data collection. The diffraction patterns were recorded under the following conditions: 45 kV anode voltage, 40 mA anode current, a step size of 0.013°, and a 2θ scan in the range of 15° to 70°. For qualitative analysis, the XRD patterns were compared with standard patterns from the ICDD database PDF-2 (PDF-2 RELEASE 2024) using HighScore Plus software (Malvern PANalytical, UK).

Film morphology and elemental analysis were investigated using the Verios G4 HP, a Scanning Electron Microscope with a Schottky FEG electron source, SE and BSE detectors, and the Oxford Instruments AZtec Live, Ultim Max SDD 65 mm^2 EDS detector. The samples were prepared for SEM measurements with Balzers SCD 050 – carbon coated with a 5–10 nm layer of carbon via carbon thread evaporation. Fourier transform infrared (FTIR) spectra of the fabricated films were recorded on a Spectrum One spectrometer (Perkin Elmer) in the range of 4000 to 400 cm^{-1}. Raman spectra were recorded with a Raman spectrometer (NTEGRA Spectra, NT-MDT Inc.). The optical properties were investigated through UV–Vis absorption spectroscopy, which was performed in transmission mode using an Ocean Optics HR4000 UV–Vis spectrophotometer with a 150 W Xe light source.

The chemical composition of fabricated thin films was examined using X-ray photoelectron spectroscopy (XPS) with a SPECS system, equiped with a Phoibos100 electron energy analyzer and a monochromatized X-ray source operating at 1486.74 eV. During the

This preprint research paper has not been peer reviewed. Electronic copy available at: https://ssrn.com/abstract=5365557

measurements, the pressure in the XPS chamber was maintained at approximately 10^{-9} mTorr. Photoemission spectra around the Bi 4f, V 2p, and O 1s core-levels were acquired with an electron pass energy of 10 eV, while the pass energy of 25 eV was used for the valence band spectra. All spectra were calibrated according to the C 1s peak, set at a binding energy (BE) of 285.0 eV. The core–level photoemission spectra were numerically fitted with the UNIFIT program [27], using a combination of Gaussian and Lorentzian functions with Shirley background subtraction.

2.3 PEC characterization

The photoelectrochemical (PEC) properties of the prepared Bi_2O_3–$BiVO_4$ thin films were studied using a MultiEMStat4, a multi–channel potentiostat / galvanostat / impedance analyzer. The data were analyzed using the MultiTrace software, which controls and manages the individual channels of multi-channel instruments. The Bi_2O_3–$BiVO_4$ thin films were used as the working electrode while a Pt coil and Ag/AgCl were used as the counter and reference electrodes, respectively. Open circuit potential (OCP) and linear sweep voltammetry (LSV) were studied in Na_2SO_4 (0.1 M) electrolyte [28, 29] in the dark and under illumination using an AM 1.5 G solar simulator (Solar Light Co.) with the light intensity set to 1 sun (100 mW/cm²), verified using a standard silicon photodiode. The surface area of the working electrode exposed to the electrolyte was approximately 1 cm^2. Electrochemical impedance spectroscopy (EIS) measurements were also performed both in the dark and under illumination, using an alternating perturbation with an amplitude of 10 mV over a frequency range of 0.1 Hz to 100 kHz.

3.Results and discussion

3. 1 Effect of reactive magnetron co-sputtering parameters and annealing temperature on the tuning of the phase composition of the thin films

In the magnetron co-sputtering process in a reactive atmosphere, the final phase composition is significantly influenced by the deposition parameters and post–deposition thermal treatment. The formation of the oxides occurs through a sequence of physical and chemical interactions between the sputtered species and the reactive atmosphere. In the case of Bi_2O_3, the oxidation process follows direct gas–phase reactions and the formation of Bi_2O_3 occurs through the oxidation of sputtered Bi species [30]. Similarly, the formation of $BiVO_4$ can be the direct oxidation reaction of Bi and V species with oxygen in the plasma environment or involves the simultaneous deposition of Bi and V atoms, followed by their reaction with oxygen. Then the resulting phase composition is highly dependent on the oxygen partial pressure and the relative deposition rates of Bi and V, which are controlled by the sputtering power applied to each target. In addition, annealing after deposition in air generally increases the oxygen concentration in the film, which is expected to result in the formation of different oxides, depending on the annealing temperature. $BiVO_4$ and Bi_2O_3 exist in different polymorphic forms, such as monoclinic scheelite, tetragonal scheelite, and tetragonal zircon for $BiVO_4$ [31], and α–, β–, γ–, ω–, δ–phases for Bi_2O_3 [32, 33], each exhibiting different structural, optical, and photocatalytic properties.

This preprint research paper has not been peer reviewed. Electronic copy available at: https://ssrn.com/abstract=5365557

The phase composition of the films after annealing at 400 °C in air was investigated with the ex-situ HT–GIXRD analysis for a wide range of deposition parameters (**Table S1**), while the phase transitions and the development of different crystallographic phases during the in-situ annealing process were investigated with the HT–GIXRD experiments on selected group of samples. HT–GIXRD analysis revealed that the amorphous thin films were obtained after the deposition while annealing at 400 °C results in crystallographic structure(s) that depends on the deposition rates of meatallic targets, expressed as the ratio of measured target currents (I_V/I_{Bi}), and on the flow of O_2 reactive gas. The target current is the measure of the sputtered material from the target and it is related to the applied power to the target. **Figure 1** presentsHT-GIXRD patterns of representative thin films synthesized under varying I_V/I_{Bi} ratios. At relatively low vanadium deposition rates ($I_V/I_{Bi} \leq 10$), the films primarily consist of the β-Bi_2O_3 phase (ICDD PDF 01-076-0147; space group P–421c; a = b = 7.7380 Å, c = 5.7310 Å), with minor traces of tetragonal $BiVO_4$ (ICDD PDF 01-075-2481; space group $I4_1/a$; a = b = 5.1470 Å, c = 11.7216 Å) observed (see BO–1 to BO–4 in **Table S1**). As the I_V/I_{Bi} ratio increases, more vanadium atoms become available, leading to an increase in the $BiVO_4$ fraction and a decrease in the Bi_2O_3 fraction. The Bi_2O_3–$BiVO_4$ phase composition is successfully obtained when the I_V/I_{Bi} ratio is in the range of 10 – 14.9 (see BO/BVO–1 to BO/BVO–5 in **Table S1**). However, if the I_V/I_{Bi} ratio exceeds a critical threshold value, which is typically 15 in our experiment, $BiVO_4$ becomes the predominant or only phase present. Compared to the influence of the deposition rates, the influence of the O_2 flux on the phase composition appears to be much smaller. Our results are in agreement with a recent study on the preparation of pure $BiVO_4$ thin films by magnetron co-sputtering, where similar deposition conditions were described to achieve a Bi:V molar ratio of 1:1 [17]. In addition, increasing the deposition rate of Bi was reported to promote a Bi–rich composition [17], a strategy that was also used in our study to obtain the Bi_2O_3–$BiVO_4$ heterojunction composite.

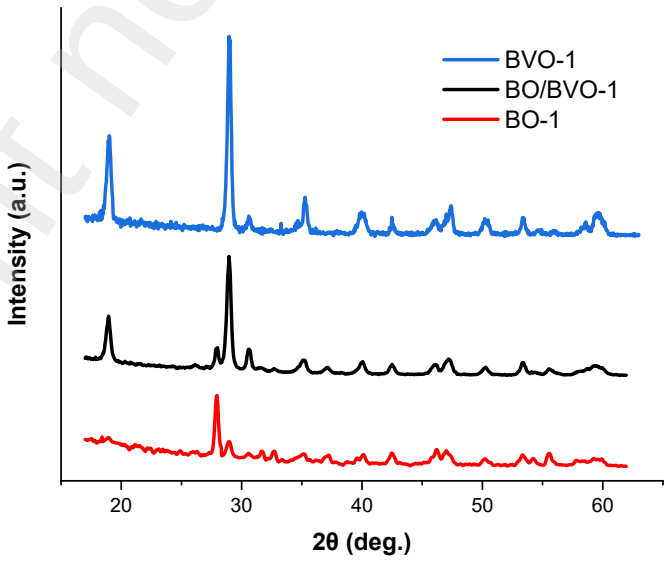

Figure 1. GIXRD for BO-1, BO/BVO-1 and BVO-1 samples.

Preprint not peer reviewed

This preprint research paper has not been peer reviewed. Electronic copy available at: https://ssrn.com/abstract=5365557

In addition to magnetron deposition parameters, the crystalline phase composition of the resulting Bi_2O_3–$BiVO_4$ thin films can be further controlled through post-deposition annealing. For example, varying the annealing temperature alters the phase evolution in films deposited at I_V/I_{Bi} = 11.52 (BO/BVO–1; see **Figure 2**). At lower temperatures, the diffraction peaks correspond to a hexagonal bismuth phase (ICDD PDF 00-005-0519, space group R-3M, a=b=4.5460 A and c =11.8600 A), indicating initial crystallization of metallic Bi. As the temperature increases to 250–450 °C, the film transitions into a mixed-phase composition of Bi_2O_3 and $BiVO_4$. Upon annealing at 500 °C and above, the formation of a single-phase $BiVO_4$ becomes dominant, reflecting enhanced phase purity and crystallinity. Similarly, the BO/BVO–5 sample (deposited at I_V/I_{Bi} = 14.92; see **Figure S2**) shows comparable phase evolution with annealing.

The HT-GIXRD results clearly show the progressive phase evolution during thermal treatment (see also **Figure S2** for sample BO/BVO–5, in T**able S1**, deposited at I_V/I_{Bi} = 14.92). At lower annealing temperatures, the diffraction maxima correspond to the hexagonal Bismuth phase (ICDD PDF 00-005-0519, space group R-3M, a=b=4.5460 A and c =11.8600 A). At higher annealing temperatures between 200 and 450 °C, Bi_2O_3–$BiVO_4$ phase composition was found. Finally, at annealing temperatures of 500 °C and above, a pure phase $BiVO_4$ film develops.

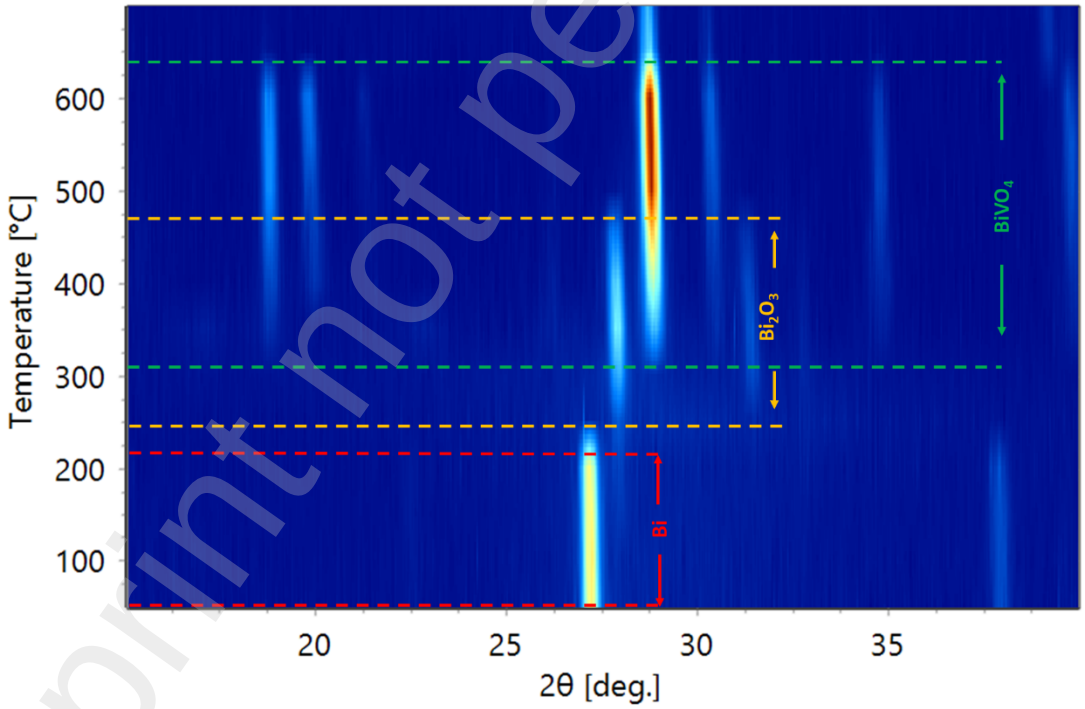

Figure 2.HT-XRD patterns (selected range of °2θ) of BO/BVO-1 in the temperature range from 50 to 650 °C.

This preprint research paper has not been peer reviewed. Electronic copy available at: https://ssrn.com/abstract=5365557

3.2.Material characterization

SEM was used for surface morphology characterization of fabricated thin films (**Figure 3 and S3**). As can be seen in **Figure 3A**, the surface of the bare FTO substrate consists of relatively large, well-defined, polygonal grains with sharp edges and clearly visible grain boundaries. The SEM images of prepared thin films show clear morphological differences between the samples examined. BO–1–4 exhibits a similar morphology, which differs from that of BO/BVO–1–5 and BVO–1. The surface morphology of BO–1, BO/BVO–1, and BVO–1 thin films is compared here as a sample of each category. BO samples comprise a very thin layer that smooths out the underlying FTO grains rather than displaying distinct grain clusters (**Figure 3B**). Interestingly, BO/BVO–1 (**Figure 3C**) showed different patterns, with nanowires produced as a structure on the top of the thin films (also see BO/BVO-2 and 5 in **Figure S3**). while BVO–1 (**Figure 3D**) exhibits a typical wormlike grain morphology commonly observed in $BiVO_4$-based materials [34]. These variations can be aligned with the phase composition identified through XRD analysis, indicating a relationship between structural evolution and phase distribution across the thin films with different dominant phases.

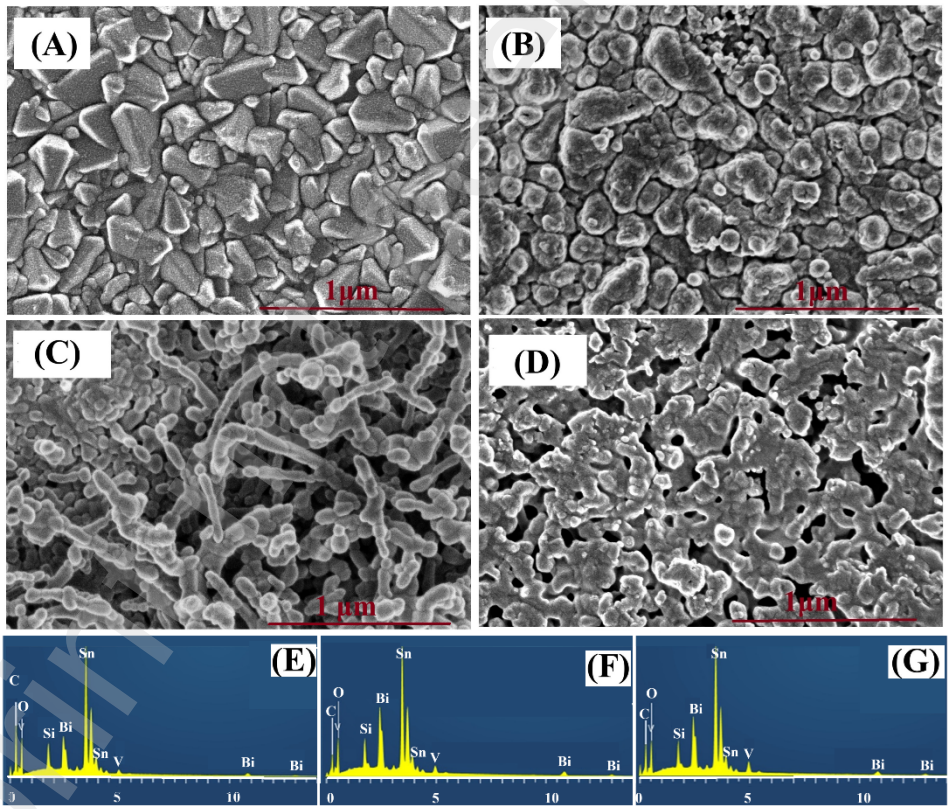

Figure 3. SEM top view images and EDX of fabricated thin films on the FTO-glass substrate (A), comparing BO-3 (B and E), BO/BVO-1(C and F), and BVO-1 (D and G) as sample of thin films with dominant-Bi_2O_3, Bi_2O_3-$BiVO_4$ p-n heterojunction, and dominant-$BiVO_4$, respectively.

This preprint research paper has not been peer reviewed. Electronic copy available at: https://ssrn.com/abstract=5365557

The analysis of the elemental composition by EDX further supports the phase distribution observed in the XRD results. As can be seen in **Figures 3E-G**, all as-prepared thin films contain the elements Bi, V, and O. In addition, Sn and Si from the substrate, as well as traces of C were detected. However, the Bi/V ratio varies between the fabricated thin films (**Table S2**). BOs thin films show higher Bi/V atomic % ratios, exceeding 2.4 and in some cases approaching pure Bi_2O_3, indicating a bismuth oxide-rich phase. In contrast, BO/BVOs thin films exhibit Bi/V atomic % ratios in the range of approximately 1.2–2.4, suggesting a composite structure of both $BiVO_4$ and Bi_2O_3. BVO–1, on the other hand, has a Bi/V ratio close to 1, indicating a composition richer in $BiVO_4$. These structural/composition differences, which are influenced by the synthesis conditions in RMS, can have a significant impact on the optical and electrochemical properties of the material.

Further structural characterization of the fabricated thin film was carried out using FTIR analysis, with the results summarized in the Supplementary Information (**Figure S4**). The recorded FTIR spectra show no significant differences between the thin films and all exhibit the characteristic IR band in the range of 700 cm^{-1} to 900 cm^{-1} [5]. Moreover, a small band at ~ 420 cm^{-1} and a broad peak at 530–590 cm^{-1}, attributed to the stretching vibrational mode of the Bi–O bond, were detected mainly in BOs thin films, with their intensity slightly decreasing in the other samples [35]. Low-intensity bands in the 1200–1700 cm^{-1} region (**Figure S4**) were observed in some samples, indicating trace organic impurities adsorbed on the surface [5].

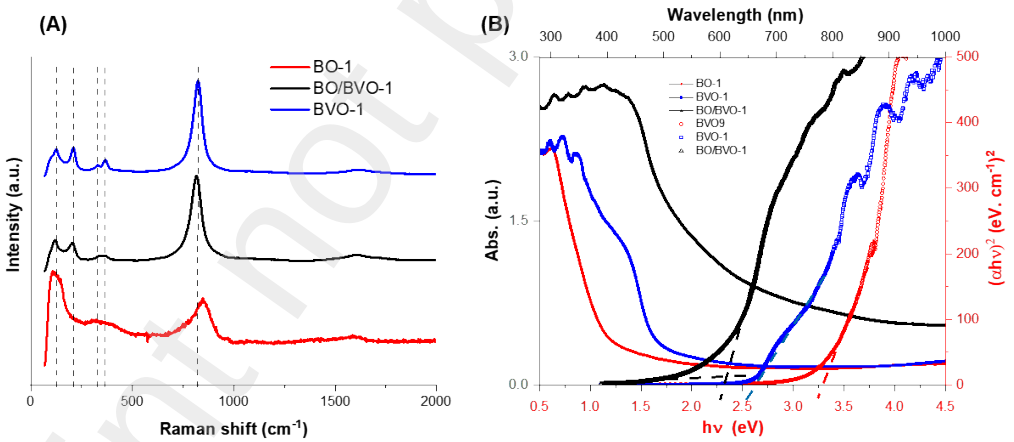

Figure 4. RAMAN spectra (including the V–O symmetric stretching mode (v_1) and the bending vibration modes (v_2 and v_4) of the VO_4 tetrahedron) (A) and UV-vis absorption spectra and Tauc plot analysis of BO-1, BVO-1, and BO/BVO-1 thin films.

Raman spectroscopy confirms the presence of both $BiVO_4$ and Bi_2O_3 phases in the thin films. Characteristic $BiVO_4$ vibrational modes are clearly observed, including the strong V–O symmetric stretching mode (v_1) of the VO_4 tetrahedron around 828 cm^{-1} (**Figures 4A and S5A**) [36]. The doublet peaks at 328 cm^{-1} and 369 cm^{-1} correspond to the bending vibrations (v_2 and v_4) of the VO_4 group [33, 34]. Additional low-frequency modes at 127.6 cm^{-1} and 210.9

This preprint research paper has not been peer reviewed. Electronic copy available at: https://ssrn.com/abstract=5365557

cm^{-1} are attributed to lattice vibrations, primarily representing external rotational and translational motions of Bi and VO_4 units [37-39]. In Bi_2O_3-dominant films, notable shifts and changes in Raman peak intensities suggest local structural distortions and increased Bi_2O_3 incorporation. Detailed analysis of vibrational mode shifts and phase interactions is provided in the Supplementary Information.

UV-Vis measurements were performed to determine the optical properties of fabricated thin films. The absorption data are shown in **Figure 4B,** where distinct differences in the absorption spectra among the thin films can be observed. The band gaps of pristine $BiVO_4$ and Bi_2O_3 were reported to be 2.5±0.4 eV and 2.8±0.4 eV, respectively [5, 40]. The band gaps of our thin films were determined using the Tauc plot, i.e. using the baseline approach and curve extrapolation [41] (see **Figures 4B** and **S5B and C**), and assuming that $BiVO_4$ and Bi_2O_3 have a direct band gap. The resulting values are 3.26, 3.16, 3.07, and 3.18 eV for BO–1 to BO–4, respectively. A band gap of 2.58 eV was estimated for BVO–1, while the BO/BVO–1 to BO/BVO–5 samples exhibited band gaps of 2.41, 2.49, 2.56, 2.61, and 2.58 eV, respectively. These variations can be attributed to differences in the dominant crystalline phases present in the fabricated thin films (**Table S1**).

The different phases observed in annealed films indicate significant changes in the atomic oxidation states and surface chemistry, which are crucial for the photocatalytic behaviour of these materials. To further investigate these properties, the chemical environments of Bi, V and O atoms in the Bi_2O_3 –dominant phase and Bi_2O_3–$BiVO_4$ films as well as in Bi_2O_3–$BiVO_4$ heterojunction films were studied under different annealing conditions using XPS. This enabled a detailed correlation between structural transitions and electronic surface states.

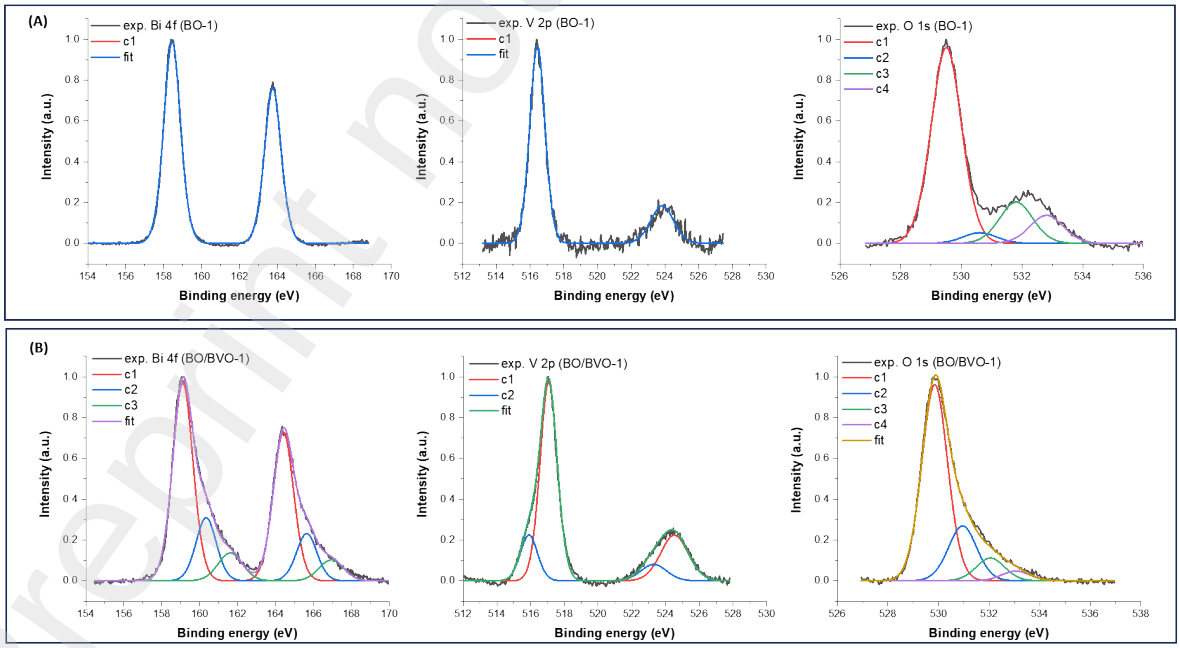

This preprint research paper has not been peer reviewed. Electronic copy available at: https://ssrn.com/abstract=5365557

Figure 5. Photoemission spectra around Bi 4f, V 2p and O 1s core-levels measured from the surfaces of BO-1 (A) and BO/BVO-1 (B) samples. Experimental curves are fitted with the product of Gaussian and Lorentzian functions.

XPS survey spectra of selectred thin films annealed at 400 °C are shown in **Figure S6,** revealing the presence of Bi, O and V in synthesized films, together with the adventitious surface carbon. **Figures 5 and S7** show the high-resolution XPS spectra around the Bi 4f, V 2p and O 1s core-levels measured at the surfaces of Bi_2O_3 dominant and Bi_2O_3–$BiVO_4$ heterojunction thin films.

In the case of BO-1, the XPS spectra around Bi 4f show two main peaks at 158.4 eV and 163.75 eV, which correspond to the Bi 4f7/2-4f5/2 doublet and indicating the presence of Bi in the 3+ oxidation state. The photoemission corresponding to the V 2p3/2-2p1/2 doublet is relatively weak, suggesting a very low vanadium content. A calculation estimates a surface composition of approximately O: 33.9 %, Bi: 19.2 % and V: 3.4 %, with the remainder being adventitious carbon in the BO-1 sample.

In all selected Bi_2O_3–$BiVO_4$ heterojunction thin films, the Bi 4f spectra exhibit asymmetric peaks, indicating a contribution from Bi atoms in different oxidation states. The Bi 4f experimental curve can be satisfactorily fitted with three well-resolved doublets that are shifted in binding energy (BE). We attribute the most pronounced doublet (with the Bi 4f7/2 peak at the BE of 159.0 eV) to Bi^{3+} ions in $BiVO_4$ and Bi_2O_3 crystallites. On the other hand, the doublet shifted by 1.3 eV towards higher BEs can be attributed to $BiVO_4$ in the vicinity of Bi_2O_3, i.e. it indicates the formation of Bi_2O_3–$BiVO_4$ heterojunctions. Namely, a similar shift was observed in the Bi 4f spectra of $BiVO_4$, with the creation of the heterostructures consisting of $BiVO_4$ and p–type semiconductor such as $ZnIn_2S_4$ [42], CuS [43] or $NiCoO_2$ [44]. Finally, the third doublet, which is shifted by 2.5 eV with respect to the main Bi^{3+} doublet (observed in BO/BVO-1 and BO/BVO–3 samples) can be attributed to the formation of the Bi^{5+} oxidation state. The photoemission spectra from V 2p core-levels are fitted with two doublets, with the energy difference of 7.4 eV between V $2p_{3/2}$ and V $2p_{1/2}$ peaks. These spectra show that vanadium is mainly present as V^{5+} (main doublet with the V $2p_{3/2}$ peak at 516.7 eV), but the V^{4+} oxidation state (with the V $2p_{3/2}$ peak at 515.6 eV) is also present in all samples. In addition, the O 1s spectra show that a large amount of oxygen-related defects are present in all Bi_2O_3–$BiVO_4$ films. Besides the main peak at the BE of 530.0 eV related to lattice oxygen (O^{2-} ions in $BiVO_4$ and Bi_2O_3 matrices), peaks due to O vacancies (531.0 eV), and O-H groups/O interstitials (532.2 eV) show large intensities in all O 1s spectra.

To investigate the influence of annealing temperature on the oxidation states of Bi–, V– and O–atoms, we performed XPS measurements on BO/BVO–5 sample annealed at 250 °C, 450 °C and 550 °C (see **Figure 6**). A small contribution from the metallic Bi state (represented by a doublet shifted by -2.2 eV in relation to Bi^{3+}) is present only in BO/BVO-5 film before annealing (see **Figure 6A**). The oxygen-related impurities/defects and the V^{4+} oxidation state of vanadium are present in the 250 °C annealed sample. However, after

This preprint research paper has not been peer reviewed. Electronic copy available at: https://ssrn.com/abstract=5365557

annealing at 450 and 550 °C, these defects are significantly reduced. In addition, the Bi-4f doublet at 250 °C shows a complex structure, which in turn disappears after annealing at 450 and 550 °C. At these temperatures, bismuth and vanadium are only present as Bi^{3+} and V^{5+} species, respectively. Moreover, a doublet related to Bi_2O_3-$BiVO_4$ heterojunctions is missing in the corresponding Bi-4f spectra, indicating the formation of pure $BiVO_4$, which is consistent with the high-temperature XRD measurements. Therefore, high temperature annealing can significantly reduce the amount of defects in Bi_2O_3-$BiVO_4$ samples, leading to the formation of only $BiVO_4$ phase in the annealed films.

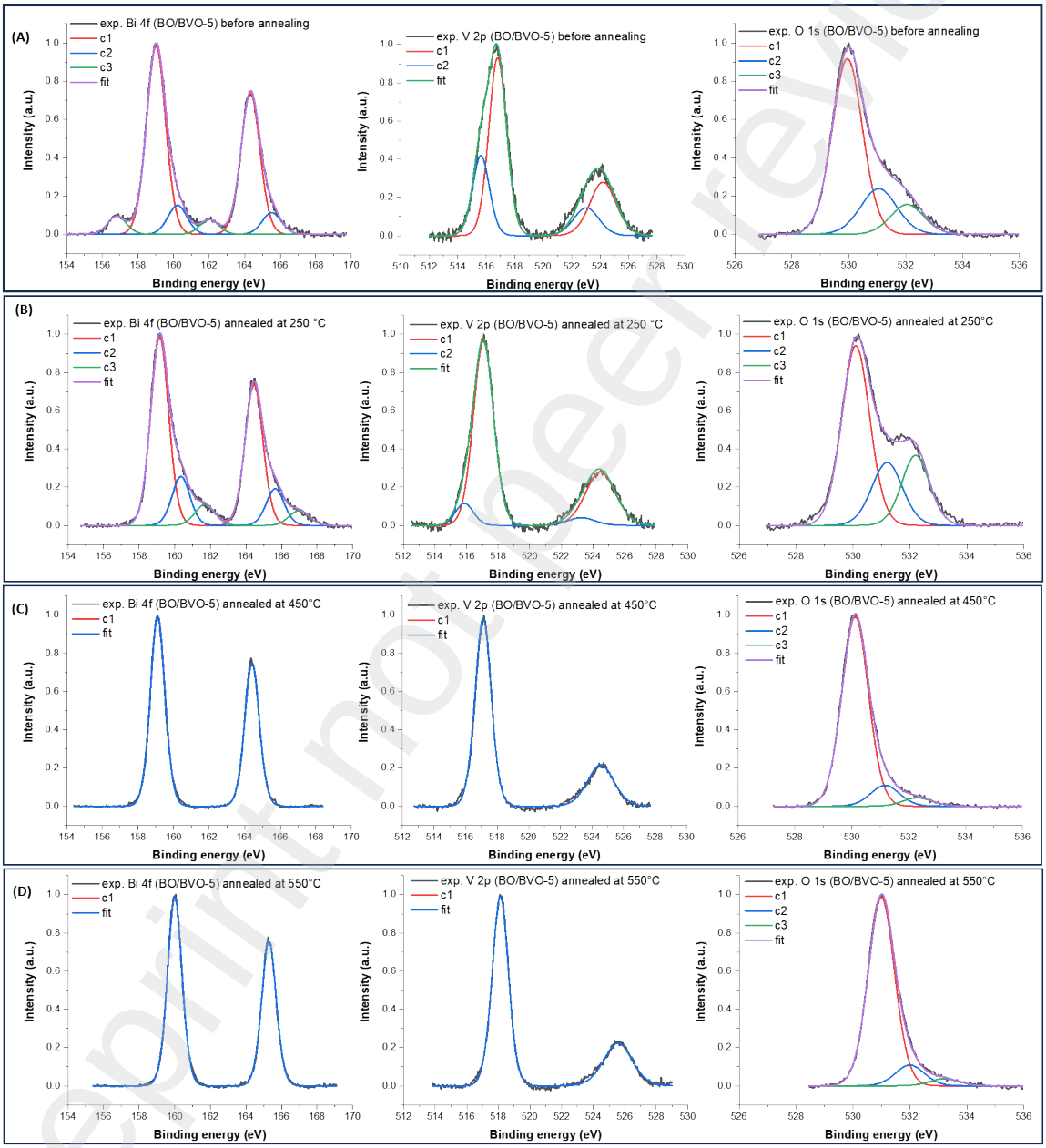

Figure 6. Photoemission spectra around Bi 4f, V 2p and O 1s core-levels measured from the surfaces of BO/BVO-5, before annealing (A) and after annealing at different temperatures: 250 °C (B), 450 °C (C) and 550 °C (D). Experimental curves are fitted with the product of Gaussian and Lorentzian functions.

This preprint research paper has not been peer reviewed. Electronic copy available at: https://ssrn.com/abstract=5365557

The valence band (VB) spectra of the BO/BVO–1 and BO–1 samples were analysed (**Figure 7)**. In the case of BO/BVO–1, the energy difference between the Fermi level and the VB maximum is about 1.87 eV, indicating an n–type behaviour. In contrast, the Fermi level of the BO–1 sample is much closer to the VB maximum (~1.04 eV), indicating a p–type nature of this sample. This is in good agreement with the literature, which suggests that Bi_2O_3 is a p-type semiconductor [38]. On the other hand, pure $BiVO_4$ is an n-type semiconductor with a Fermi level that is 1.68 eV more positive than its VB maximum [2]. Consequently, the Bi_2O_3–$BiVO_4$ heterojunction will redistribute the charge at the interface until the Fermi levels of the two matrials equlibriate. The result is a band bending and the formation of an electric field at the interface, similar to the well known p–n junction. Given the Bi_2O_3–$BiVO_4$ composition and the RMS fabrication method, we propose that nanoscale p–n junctions could form throughout the films, resulting in enhanced local band bending and improved charge separation. To evaluate how this heterojunction influences e-/h+ recombination and the photocatalytic performance of the Bi_2O_3–$BiVO_4$ photoanode, further PEC measurements were conducted.

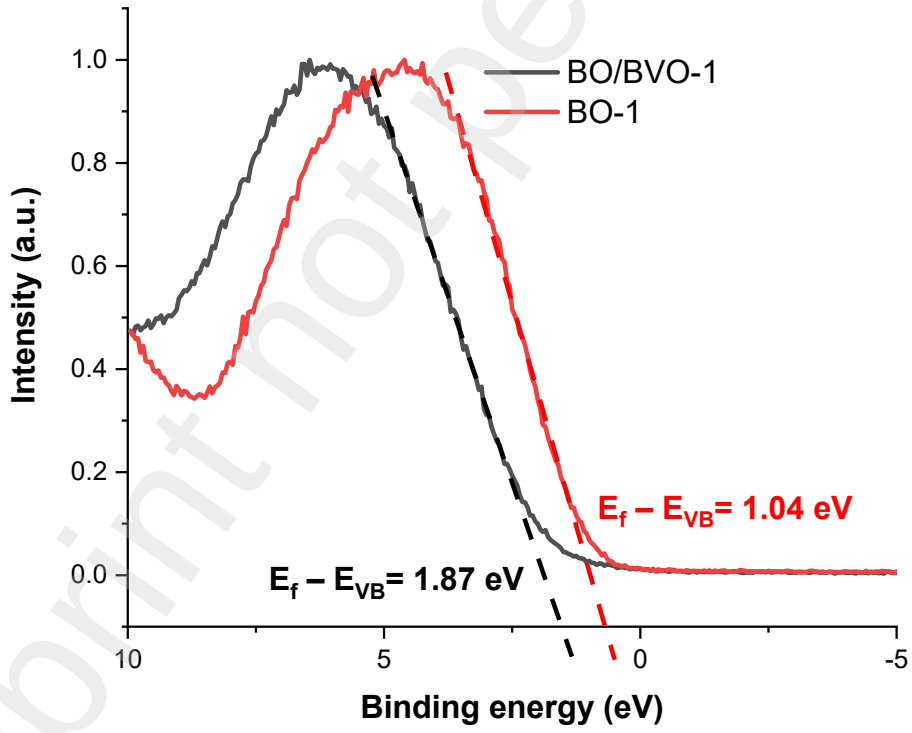

Figure 7. The photoemission spectra around valence band states for BO-1 and BO/BVO-1 thin films.

Preprint not peer reviewed

This preprint research paper has not been peer reviewed. Electronic copy available at: https://ssrn.com/abstract=5365557

3.3 Photoelectrochemical characterization

PEC characterization of all fabricated thin films is provided in the Supplementary Information. Here, the results of BO–1, BVO–1, and BO/BVO–1 are compared as representative examples of three categories: Bi_2O_3-dominant, pure $BiVO_4$, and Bi_2O_3–$BiVO_4$ heterojunction thin films, respectively. This comparison highlights the effect of the Bi_2O_3–$BiVO_4$ heterojunction on PEC performance relative to Bi_2O_3-dominant and pure $BiVO_4$ films.

The photovoltage, i.e. the difference of the OCP in the dark and in the light, is an important parameter for evaluating the photocatalytic performance as it reflects the equilibrium potential of a photoelectrode under illumination without external bias. A change in the OCP value after switching on the light reflects the generated photovoltage which represents the difference of the Fermi quasi-levels of holes (Ef,p) and electrons (Ef,n) and is directly related to the steady-state concentration of photogenerated charge carriers in the semiconductor [45]. Under illumination, the quasi-Fermi level in the n-type region shifts to more negative potentials, as evidenced by a stable negative photovoltage shift, an indicator of efficient electron accumulation and extraction. On the other hand, a positive OCP shift after switching on the illumination reflects a cathodic behavior associated with p–type materials.

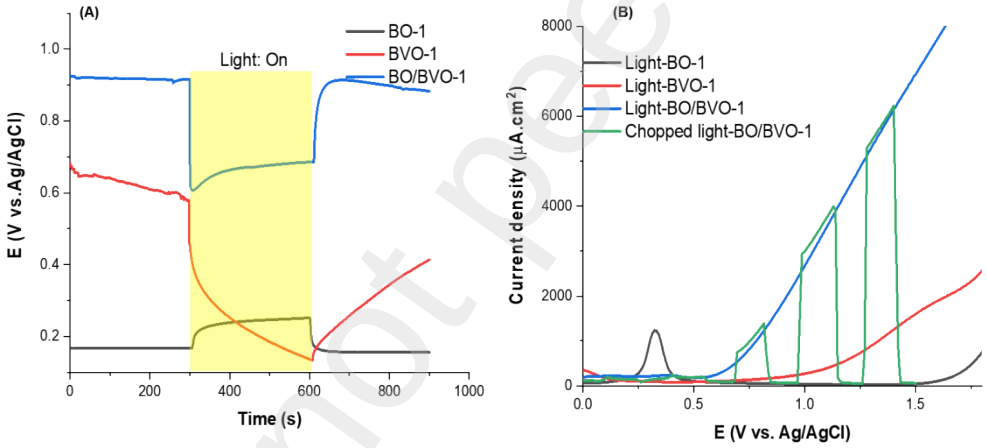

Figure 8. OCP (A) and LSV plots(scan rate 20 mV/s) (B) of BO-1, BVO-1, and BVO-1 thin films in Na_2SO_4 (1M).

BO–1–4, which is rich in Bi_2O_3, exhibits a positive OCP shift (**Figures 8A and S8**), indicating a p–type character of Bi_2O_3, in agreement with the XPS results (see **Figure 7**). However, the photovoltage of this sample is relatively low, suggesting a poor charge separation efficiency, i.e. high recombination rate. In contrast, the $BiVO_4$ thin film (BVO–1), shows a negative OCP shift, which is consistent with the typical n-type behavior of semiconductors (**Figure 8A)**. However, its OCP is unstable under illumination which could be due to strong e^-/h^+ recombination and ineffective hole extraction. Interestingly, the Bi_2O_3–$BiVO_4$ heterojunction thin film also exhibits n–type behavior, moderate photovoltage generation (~0.25 V) and more stable behavior (**Figures 8A and S8)**. The rapid stabilization of the photovoltage in the BO/BVO–1 film can be attributed to the formation of a p–n

This preprint research paper has not been peer reviewed. Electronic copy available at: https://ssrn.com/abstract=5365557

heterojunction at the Bi_2O_3 / $BiVO_4$ interface, where the built-in electric field promotes the spatial separation of photogenerated charge carriers and thus reduces the recombination.

The BO–1–4 thin films, which are Bi_2O_3-dominant, also exhibited the lowest photocurrent densities among all fabricated samples, consistent with their low photovoltage (**Figure 8B**). In contrast, all BO/BVO composite thin films (except BO/BVO–3) demonstrated higher photocurrent densities than the BVO–1 sample (**Figures 8B and S9**). These films also showed an increase in photocurrent with increasing anodic bias, which may be attributed to enhanced band bending at the semiconductor/electrolyte interface that improves charge separation and reduces recombination [46]. More importantly, BO/BVO–1 achieved the highest photocurrent density, exceeding that of BVO–1 by 2.5 – to 10 times, depending on the applied voltage.

The enhanced photocurrent observed in BO/BVO–1, which contains a mixture of Bi_2O_3 and $BiVO_4$ phases, can be attributed to the formation of a p–n heterojunctions, as already anticipated in the context of the XPS results. Namely, Bi_2O_3 is an intrinsic p-type semiconductor and its Fermi level is more positive than the Fermi level of $BiVO_4$, which is an intrinsic n–type semiconductor. When these two materials are in contact, band bending and an electric field are formed at the interface due to Fermi level equilibration, as schematically shown in **Figure 9**. This electric field can promote the separation of the photogenerated charges and prevent the recombination of conduction electrons from $BiVO_4$ and valence band holes from Bi_2O_3, consistent with a type-II band alignment. In addition, the valence band maximum (VBM) of Bi_2O_3 becomes more negative than the VBM of $BiVO_4$, which is an additional driving force for the effective separation of the holes formed in $BiVO_4$. When these two effects are present at the surface of the Bi_2O_3–$BiVO_4$ photoanode, they are critical for keeping surface holes from recombination during charge transfer process. A transfer of four holes across the SEI for the production of one oxygen molecule is a relatively slow process; therefore, it is crucial to form more and longer-lived active sites for the adsorbed water oxidation intermediates (OH-ad, O_2-ad, etc.). By forming p–n heterojunctions at the surface, recombination at the surface is significantly reduced, leading to a much higher photocatalytic activity of the Bi_2O_3–$BiVO_4$ photoanode.

The LSV measurements also reveal distinct oxidation features depending on film composition (**Figure S9**). Bi_2O_3-dominant films exhibited two oxidation peaks around –0.1 V and 0.3 V vs. Ag/AgCl, while the 0.3 V peak disappeared in $BiVO_4$-dominant and its intensity decreased in Bi_2O_3–$BiVO_4$ heterojunction films. This peak can be attributed to Bi^{3+}/Bi^{5+} redox transitions commonly reported in Bi_2O_3 polymorphs [44,45]. Its suppression upon vanadium incorporation suggests stabilization of Bi in the +3 oxidation state. Meanwhile, the persistence of the –0.1 V peak may arise from vanadium redox processes, consistent with partial V^{5+} reduction observed in the XPS data [46].

This preprint research paper has not been peer reviewed. Electronic copy available at: https://ssrn.com/abstract=5365557

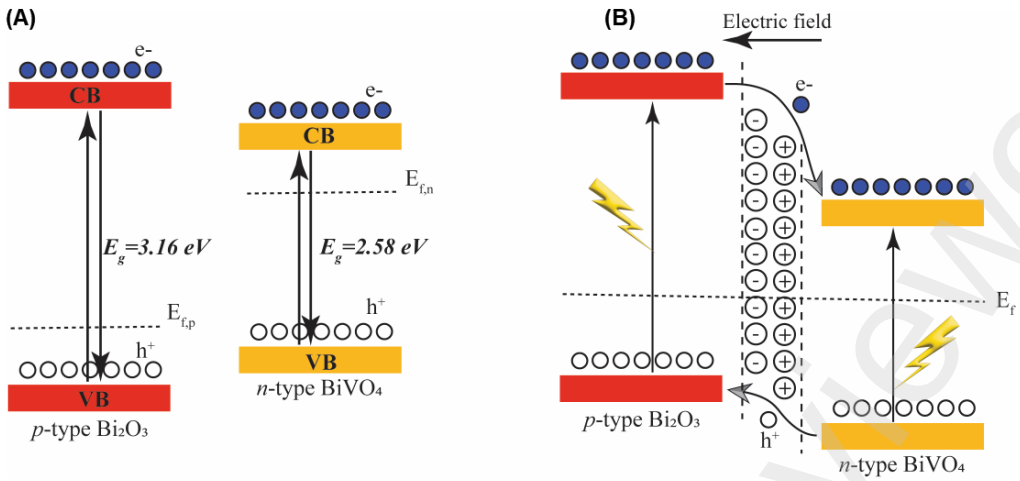

Figure 9. The schematic diagram of the energy band structure for separate phases (A) and in Bi_2O_3-$BiVO_4$ p-n heterojunction(B).

Electrochemical impedance spectroscopy was performed at bias voltages from 0.2 to 1.4 V vs. Ag/AgCl to investigate charge transport and interfacial processes. Nyquist plots (**Figure S11**) show that the BO/BVO–1 heterojunction exhibits the smallest semicircle radius, indicating the highest conductivity among the samples, consistent with LSV results. Corresponding Bode plots (**Figure S12**) reveal a sharp phase angle decrease and a shift of the phase peak to lower frequencies for BO/BVO–1, suggesting more efficient charge transfer and improved separation of photoinduced carriers.

All impedance spectra were fitted using the electrical equivalent circuit model shown in **Figure S13**, which is often used to interpret charge transfer across the SEI [4, 47]. This model assumes three contributions to the total resistance: the charge transport resistance in the semiconductor bulk (R_{dl}), the resistance associated with charge transfer across the SEI (R_{ct}) and resudual serial resistance (R_s) (back contacts, electrolyte). The bulk and surface processes also include the capacitive behaviour, which is represented by the double layer capacitance (C_{dl}) and the surface capacitance at the electrode/electrolyte interface (C_s).

Both R_{dl} and R_{ct} show similar behaviour with applied voltage, with BO/BVO–1 showing the smallest R_{dl} and R_{ct} over the entire potential range (**Figure 10A and B**). The very low values of R_{dl} and R_{ct} emphasise the functional role of Bi_2O_3–$BiVO_4$ heterojunctions as active surface and bulk modifiers that reshape interfacial energetics and charge carrier dynamics. On the other hand, the large R_{ct} for BO–1 (dominant in Bi_2O_3) indicates sluggish kinetics and poor intrinsic conductivity, which is consistent with the LSV results that identify Bi_2O_3 as having limited photoactivity.

The double–layer capacitances (C_{dl}) show typical trends that are consistent with the increase in depletion layer width at applied potential. In the thin film with heterojunctions, this trend supports the idea that the system transitions from a capacitive regime to a regime of charge transfer at the interface at higher potentials, which is consistent with the observed reduction in Rct. Cdl is consistently higher in the Bi_2O_3–$BiVO_4$ heterojunction samples than in

This preprint research paper has not been peer reviewed. Electronic copy available at: https://ssrn.com/abstract=5365557

the dominant Bi_2O_3 and $BiVO_4$ samples (**Figure 10C**), indicating a greater accumulation of charge carriers in the semiconductor. This enhancement is likely due to the presence of nanoscale p–n junctions, which locally enhance band bending and promote the separation of electrons and holes. This Cs initially decreases at low potentials before rising at higher potentials, a trend also seen in our previous work on pristine $BiVO_4$ thin films [4], suggesting dynamic changes in surface states and charge accumulation under varying bias (**Figure 10D**).

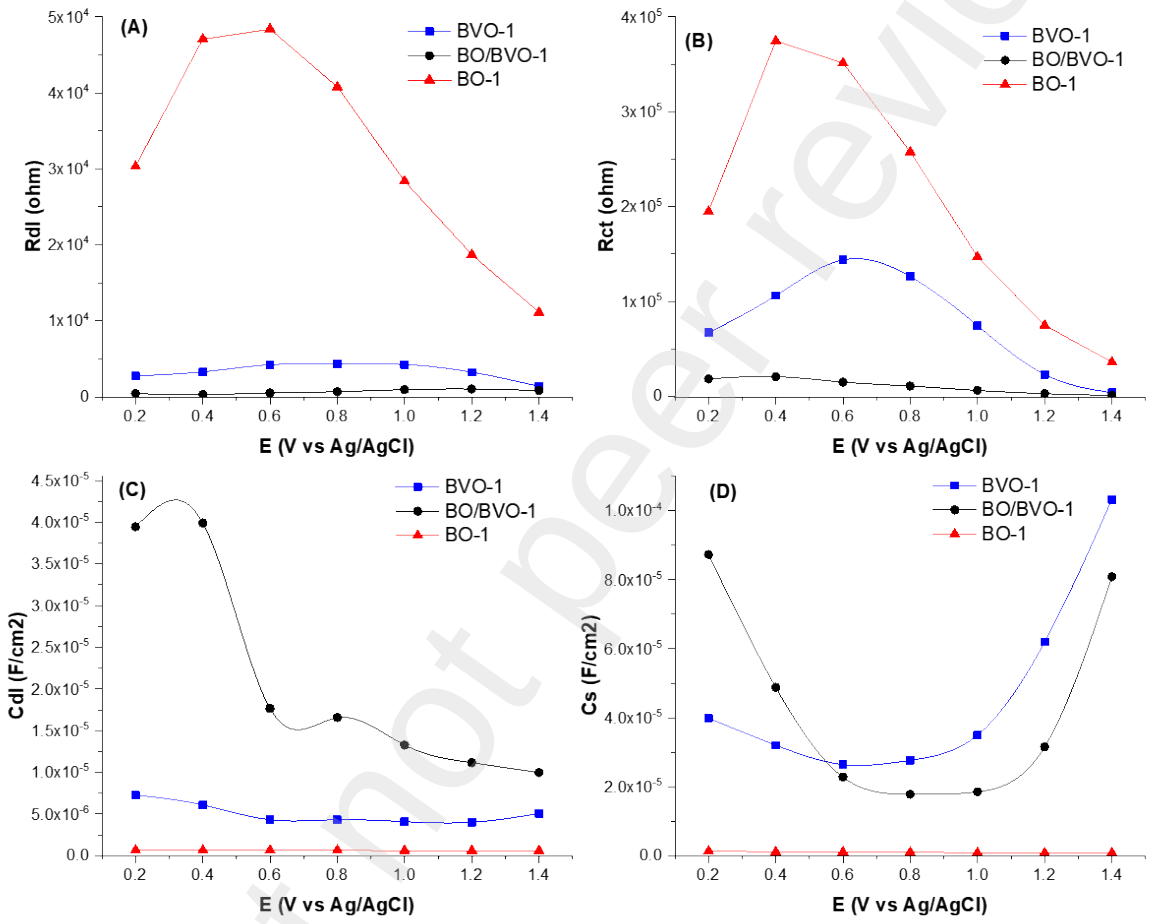

Figure 10. Elements of the equivalent circuit (FigureS10) obtained from fitting the EIS data for dominant-$BiVO_4$ (BVO-1), dominant-Bi_2O_3 (BO-1), and Bi_2O_3-$BiVO_4$ heterojunction (BO/BVO-1) photoanodes in light (A) resistance in bulk (R_{dl}), (B) charge transfer resistance (R_{ct}), (C) space charge capacitance(C_{dl}), and the surface capacitance at the electrode/electrolyte interface (C_s).

Taken together, the EIS results suggest that Bi_2O_3–$BiVO_4$ heterojunctions enhance both charge accumulation and charge transfer efficiency, which is attributed to the formation of a p–n heterojunction between p–type Bi_2O_3 and n–type $BiVO_4$ that modulates the electrostatic and electronic environment at the surface and promotes the separation of

This preprint research paper has not been peer reviewed. Electronic copy available at: https://ssrn.com/abstract=5365557

photo-generated e^-/h^+ pairs. The result is reduced recombination and improved carrier collection efficiency at the semiconductor-electrolyte interface.

Conclusion

In this study, we fabricated Bi_2O_3–$BiVO_4$ thin films by reactive magnetron co-sputtering by tuning Bi and V target powers and annealing at certain temperature to control the phase composition and interface structure. By adjusting the currents of the sputtered material, i.e. the I_V/I_{Bi} ratio, we obtained Bi_2O_3–dominant, Bi_2O_3–$BiVO_4$ heterojunction and pure $BiVO_4$ films for which the I_V/I_{Bi} ratio was set to ≤ 10, 10 < I_V/I_{Bi} ≤ 14.9 and > 15, respectively. HT–GIXRD analyses confirmed the phase evolution, thermal behavior, and formation of heterojunctions. XPS analysis revealed a p–type nature of Bi_2O_3 (Fermi level about 1.04 eV above VBM), while BO/BVO–1 showed a Fermi level about 1.87 eV above VBM, indicating band bending at the p–n junction with band alignment driven by Fermi level equilibration. This alignment creates an internal electric field at the Bi_2O_3–$BiVO_4$ interface that enhances charge separation and suppresses recombination. PEC and EIS measurements showed significantly improved photocurrent generation and lower charge transfer resistance for the heterojunction films compared to single-phase counterparts. PEC measurements confirmed the superior photoelectrochemical activity of the heterojunction films, with the highest photocurrent density being 2.5 to 10 times higher, depending on the applied bias, as compared to the $BiVO_4$ photoanode. These results highlight the role of interface engineering in optimizing photoelectrode performance for solar-driven applications.

CRediT authorship contribution statement

Tayebeh Sharifi: Conceptualization, Writing – original draft, Investigation, Formal analysis, Data Curation, Funding acquisition. **Krešimir Salamon:** Conceptualization, Investigation, Formal analysis, Writing – review & editing. **Tecush Mohammadi**: Formal analysis, Visualization, Writing – review & editing. **Dražan Jozić**: Investigation, Data Curation, Formal analysis. **Robert Peter**: Investigation, Formal analysis, Writing – review & editing, Data Curation, Funding acquisition. **Bor Arah**: Investigation, **Aleš Lapanje**: Writing – review & editing, Funding acquisition. **Marko Štrok:** Conceptualization, Funding acquisition, Writing – review & editing.

Acknowledgement

This research was funded by the European Union, BPEC-DW project under the HORIZON-MSCA-2021-PF-01 program (Grant Agreement No. 101061873) and the BIOSYSMO project (Grant Agreement No. 101060211). We also acknowledge financial support from the Slovenian Research and Innovation Agency (Projects N1-0401, J7-2597, P1-0143, and P2-0075) and the University of Rijeka (Project No. 23-190).

Preprint not peer reviewed

This preprint research paper has not been peer reviewed. Electronic copy available at: https://ssrn.com/abstract=5365557

Reference

[1] M. Xu, J. Yang, C. Sun, L. Liu, Y. Cui, B. Liang, Performance enhancement strategies of bi-based photocatalysts: A review on recent progress, Chemical Engineering Journal, 389 (2020) 124402.

[2] J. Niu, X. Guo, Y. Zhang, X. Yu, B. Yao, Construction of Z-scheme Bi3O4Br/BiVO4 nanocomposites as a promising photocatalyst for organic pollutant degradation, Journal of Alloys and Compounds, (2025) 181041.

[3] J. Yang, Z. Tao, Q. Zhao, J. Li, G. Liu, Synergistic effect of FeOOH cocatalyst and Al2O3 passivation layer on BiVO4 photoanode for enhanced photoelectrochemical water oxidation, Journal of Alloys and Compounds, 1010 (2025) 177461.

[4] K. Salamon, T. Sharifi, V. Kojić, R. Peter, N. Krstulović, Surface state-driven photoelectrochemical water oxidation enhancement in reactively co-sputtered Mo-doped $BiVO_4$ photoanodes, Electrochimica Acta, (2025) 146357.

[5] T. Sharifi, D. Crmaric, M. Kovacic, M. Popovic, M.K. Rokovic, H. Kusic, D. Jozić, G. Ambrožić, D. Kralj, J. Kontrec, Tailored BiVO4 for enhanced visible-light photocatalytic performance, Journal of environmental chemical engineering, 9 (2021) 106025.

[6] P. Qiu, B. Park, J. Choi, M. Cui, J. Kim, J. Khim, BiVO4/Bi2O3 heterojunction deposited on graphene for an enhanced visible-light photocatalytic activity, Journal of Alloys and Compounds, 706 (2017) 7-15.

[7] M. Mao, F. Chen, C. Zheng, J. Ning, Y. Zhong, Y. Hu, Facile synthesis of porous Bi2O3-BiVO4 pn heterojunction composite microrods with highly efficient photocatalytic degradation of phenol, Journal of Alloys and Compounds, 688 (2016) 1080-1087.

[8] C. Murugan, A. Pandikumar, Reinforcement of visible-light harvesting and charge-transfer dynamics of BiVO4 photoanode via formation of p–n heterojunction with CuO for efficient photoelectrocatalytic water splitting, ACS Applied Energy Materials, 5 (2022) 6618-6632.

[9] C. Murugan, A.S. Mary, R. Velmurugan, B. Subramanian, P. Murugan, A. Pandikumar, Investigating the interfacial charge transfer between electrodeposited BiVO4 and pulsed laser-deposited Co3O4 pn junction photoanode in photoelectrocatalytic water splitting, Chemical Engineering Journal, 483 (2024) 149104.

[10] Y. Gao, Y. Hu, F. Liu, Y. Tian, D. Zeng, T. Shen, H. Yuan, R. Guan, J. Song, Preparation of nanofiber Co–BiVO4/Bi2O3 pn heterojunction for high efficiency photocatalytic degradation of organic pollutants, Ceramics International, 50 (2024) 5643-5656.

[11] Y.-C. Liang, S.-H. Chen, Triangular BiVO4-Bi2O3 ultrathin sheet composites for enhancement of photoelectrochemical and photocatalytic performance, Journal of Science: Advanced Materials and Devices, 9 (2024) 100730.

[12] O.F. Lopes, K.T. Carvalho, W. Avansi Jr, C. Ribeiro, Growth of BiVO4 nanoparticles on a Bi2O3 surface: effect of heterojunction formation on visible irradiation-driven catalytic performance, The Journal of Physical Chemistry C, 121 (2017) 13747-13756.

[13] N. Myung, S. Ham, S. Choi, Y. Chae, W.-G. Kim, Y.J. Jeon, K.-J. Paeng, W. Chanmanee, N.R. de Tacconi, K. Rajeshwar, Tailoring interfaces for electrochemical synthesis of semiconductor films: BiVO4, Bi2O3, or composites, The Journal of Physical Chemistry C, 115 (2011) 7793-7800.

[14] M.-L. Guan, D.-K. Ma, S.-W. Hu, Y.-J. Chen, S.-M. Huang, From hollow olive-shaped BiVO4 to n− p core− shell BiVO4@ Bi2O3 microspheres: Controlled synthesis and enhanced visible-light-responsive photocatalytic properties, Inorganic Chemistry, 50 (2011) 800-805.

[15] Y. Wu, J. Wang, Y. Huang, Y. Wei, Z. Sun, X. Zheng, C. Zhang, N. Zhou, L. Fan, J. Wu, Solvothermal synthesis of Bi2O3/BiVO4 heterojunction with enhanced visible-light photocatalytic performances, Journal of Semiconductors, 37 (2016) 083004.

[16] F. Shafiq, M.B. Tahir, A. Hussain, M. Sagir, J. ur Rehman, I. Kebaili, H. Alrobei, M. Alzaid, The construction of a highly efficient pn heterojunction Bi2O3/BiVO4 for hydrogen evolution through solar water splitting, International Journal of Hydrogen Energy, 47 (2022) 4594-4600.

[17] E.V. Kumar, T. Soundarya, B.K. Swamy, G. Nagaraju, In situ growth of BiVO4–Bi2O3 pn heterojunction nanocomposite via facile green combustion method: Efficient photocatalytic activity

This preprint research paper has not been peer reviewed. Electronic copy available at: https://ssrn.com/abstract=5365557

under visible light, photoluminescence and biosensing applications, Materials Chemistry and Physics, 317 (2024) 129187.
[18] J. Liang, Q. Liu, T. Li, Y. Luo, S. Lu, X. Shi, F. Zhang, A.M. Asiri, X. Sun, Magnetron sputtering enabled sustainable synthesis of nanomaterials for energy electrocatalysis, Green Chemistry, 23 (2021) 2834-2867.
[19] R. Garg, S. Gonuguntla, S. Sk, M.S. Iqbal, A.O. Dada, U. Pal, M. Ahmadipour, Sputtering thin films: Materials, applications, challenges and future directions, Advances in colloid and interface science, (2024) 103203.
[20] N. Khemasiri, C. Chananonnawathorn, M. Horprathum, S. Pornthreeraphat, B. Saekow, A. Pankiew, A. Bootchanont, P. Songsiriritthigul, H. Nakajima, P. Kasamechonchung, Rational Concept for Fully Designing Metal-Oxynitride Films Through Reactive Gas-Timing Magnetron Sputtering: A Case Study on Zinc Oxynitride Film, Journal of Alloys and Compounds, (2025) 182211.
[21] S. Bakhtiarnia, S. Sheibani, A. Billard, E. Aubry, M.A.P. Yazdi, Deposition of nanoporous BiVO4 thin-film photocatalyst by reactive magnetron sputtering: Effect of total pressure and substrate, Transactions of Nonferrous Metals Society of China, 32 (2022) 957-971.
[22] Q. Lu, L. Ding, J. Li, N. Wang, M. Ji, N. Wang, K. Chang, High transmittance BiVO4 thin-film photoanodes by reactive magnetron sputtering for a photovoltaic-photoelectrocatalysis water splitting system, International Journal of Hydrogen Energy, 71 (2024) 1142-1150.
[23] Y. Sun, X. Zhang, B. Sun, X. Hu, M. Zhang, Q. Gao, Q. Zhou, E. Zhu, Z. Ye, S. Gao, A room-temperature RF magnetron sputtering synthesis of amorphous Bi2O3 films for self-powered UV photodetector, Materials Science in Semiconductor Processing, 194 (2025) 109578.
[24] P.L. Popa, S. Sønderby, S. Kerdsongpanya, J. Lu, H. Arwin, P. Eklund, Structural, morphological, and optical properties of Bi2O3 thin films grown by reactive sputtering, Thin Solid Films, 624 (2017) 41-48.
[25] J. Morasch, S. Li, J. Brötz, W. Jaegermann, A. Klein, Reactively magnetron sputtered Bi2 O 3 thin films: analysis of structure, optoelectronic, interface, and photovoltaic properties, physica status solidi (a), 211 (2014) 93-100.
[26] A. Behera, N. Sharma, S. Suman, P. Swaminathan, Enhancing Electrochromic Behavior of Nickel Oxide Thin Films by Optimizing Oxygen Concentration During Room Temperature Reactive Sputtering, ChemistrySelect, 10 (2025) e02244.
[27] R. Hesse, T. Chassé, R. Szargan, Peak shape analysis of core level photoelectron spectra using UNIFIT for WINDOWS, Fresenius' journal of analytical chemistry, 365 (1999) 48-54.
[28] S.P. Berglund, D.W. Flaherty, N.T. Hahn, A.J. Bard, C.B. Mullins, Photoelectrochemical oxidation of water using nanostructured BiVO4 films, The Journal of Physical Chemistry C, 115 (2011) 3794-3802.
[29] L. Liu, M. Ruan, C. Wang, T. Zhong, M. Zhou, Z. Liu, Dual Functions of Optimized FeCo Oxyhydroxide Composition in BiVO4 Photoanodes with Bi Vacancy for Photocorrosion Inhibition and Improved Photoelectrochemical Performance, ACS Applied Materials & Interfaces, 17 (2025) 28309-28320.
[30] S.A. Beden, H.A. Dumboos, M.K. Ismael, M. Kadhim Mejbel, The Role of Annealing Treatment on Crystallographic, Optical, and Electrical Features of Bi2O3 Thin Films Prepared Using Reactive Plasma Sputtering Technology, Journal of Nanotechnology, 2023 (2023) 8638512.
[31] T. Sharifi, D. Jozić, M. Kovačić, H. Kušić, A.L. Božić, In-situ high temperature XRD study on thermally induced phase changes of BiVO4: The formation of an iso-type heterojunction, Materials letters, 305 (2021) 130816.
[32] G. Liu, S. Li, Y. Lu, J. Zhang, Z. Feng, C. Li, Controllable synthesis of α-Bi2O3 and γ-Bi2O3 with high photocatalytic activity by α-Bi2O3→ γ-Bi2O3→ α-Bi2O3 transformation in a facile precipitation method, Journal of Alloys and Compounds, 689 (2016) 787-799.
[33] S.N. Kabekkodu, A. Dosen, T.N. Blanton, 5+: A comprehensive powder diffraction file™ for materials characterization, Powder Diffraction, 39 (2024) 47-59.
[34] H. Gong, N. Freudenberg, M. Nie, R. van de Krol, K. Ellmer, BiVO4 photoanodes for water splitting with high injection efficiency, deposited by reactive magnetron co-sputtering, AIP Advances, 6 (2016).

This preprint research paper has not been peer reviewed. Electronic copy available at: https://ssrn.com/abstract=5365557

[35] C. Manoharan, R. Rammohan, R. Subramanian, V. Umashanker, Synthesis of α-Bismuth oxide nanoparticles, spectral characterization and their photocatalytic activity, Inorganic and Nano-Metal Chemistry, 53 (2023) 113-121.
[36] T.S. Dabodiya, P. Selvarasu, A.V. Murugan, Tetragonal to monoclinic crystalline phases change of BiVO4 via microwave-hydrothermal reaction: in correlation with visible-light-driven photocatalytic performance, Inorganic chemistry, 58 (2019) 5096-5110.
[37] S. Chauhan, A. Singh, R. Saini, L. Thirumalaisamy, J. Ramakrishnan, T.A. Kumaravelu, T. Rajalingam, C.-L. Dong, A. Kandasami, Regulation of oxygen vacancies by gamma-irradiation in BiVO4 thin films and their electrochemical performance, Ceramics International, (2025).
[38] V. Denisov, A. Ivlev, A. Lipin, B. Mavrin, V. Orlov, Raman spectra and lattice dynamics of single-crystal, Journal of Physics: Condensed Matter, 9 (1997) 4967.
[39] D.T. Bulut, Exploring the dual role of BiVO4 nanoparticles: unveiling enhanced antimicrobial efficacy and photocatalytic performance, Journal of Sol-Gel Science and Technology, (2025) 1-25.
[40] E. Muhammad, T. Jan, A. Jalil, Experimental and computational study of Bi2O3/WO3 heterostructures as efficient solar driven photocatalyst, Inorganic Chemistry Communications, 171 (2025) 113581.
[41] P. Makuła, M. Pacia, W. Macyk, How to correctly determine the band gap energy of modified semiconductor photocatalysts based on UV–Vis spectra, ACS Publications, 2018, pp. 6814-6817.
[42] W. Jin, X. Zhong, X. Li, K. Yang, S. Liu, R. Xie, Y. Li, 2D/3D BiVO4@ ZnIn2S4 Hierarchical Heterojunction for Enhanced One-Electron Oxygen Reduction Kinetics of H2O2 Artificial Photosynthesis, Inorganic Chemistry, (2025).
[43] C. Lai, M. Zhang, B. Li, D. Huang, G. Zeng, L. Qin, X. Liu, H. Yi, M. Cheng, L. Li, Fabrication of CuS/BiVO4 (0 4 0) binary heterojunction photocatalysts with enhanced photocatalytic activity for Ciprofloxacin degradation and mechanism insight, Chemical Engineering Journal, 358 (2019) 891-902.
[44] T. Palaniselvam, L. Shi, G. Mettela, D.H. Anjum, R. Li, K.P. Katuri, P.E. Saikaly, P. Wang, Vastly enhanced BiVO4 photocatalytic OER performance by NiCoO2 as cocatalyst, Advanced Materials Interfaces, 4 (2017) 1700540.
[45] L.I. Sorokina, A.M. Tarasov, A.I. Pepelyaeva, P.I. Lazarenko, A.Y. Trifonov, T.P. Savchuk, A.V. Kuzmin, A.V. Tregubov, E.N. Shabaeva, E.S. Zhurina, The Composite TiO2–CuOx Layers Formed by Electrophoretic Method for CO2 Gas Photoreduction, Nanomaterials, 13 (2023) 2030.
[46] M.G. Walter, E.L. Warren, J.R. McKone, S.W. Boettcher, Q. Mi, E.A. Santori, N.S. Lewis, Solar water splitting cells, Chemical reviews, 110 (2010) 6446-6473.
[47] L. Bertoluzzi, P. Lopez-Varo, J.A.J. Tejada, J. Bisquert, Charge transfer processes at the semiconductor/electrolyte interface for solar fuel production: insight from impedance spectroscopy, Journal of Materials Chemistry A, 4 (2016) 2873-2879.

Preprint not peer reviewed

This preprint research paper has not been peer reviewed. Electronic copy available at: https://ssrn.com/abstract=5365557

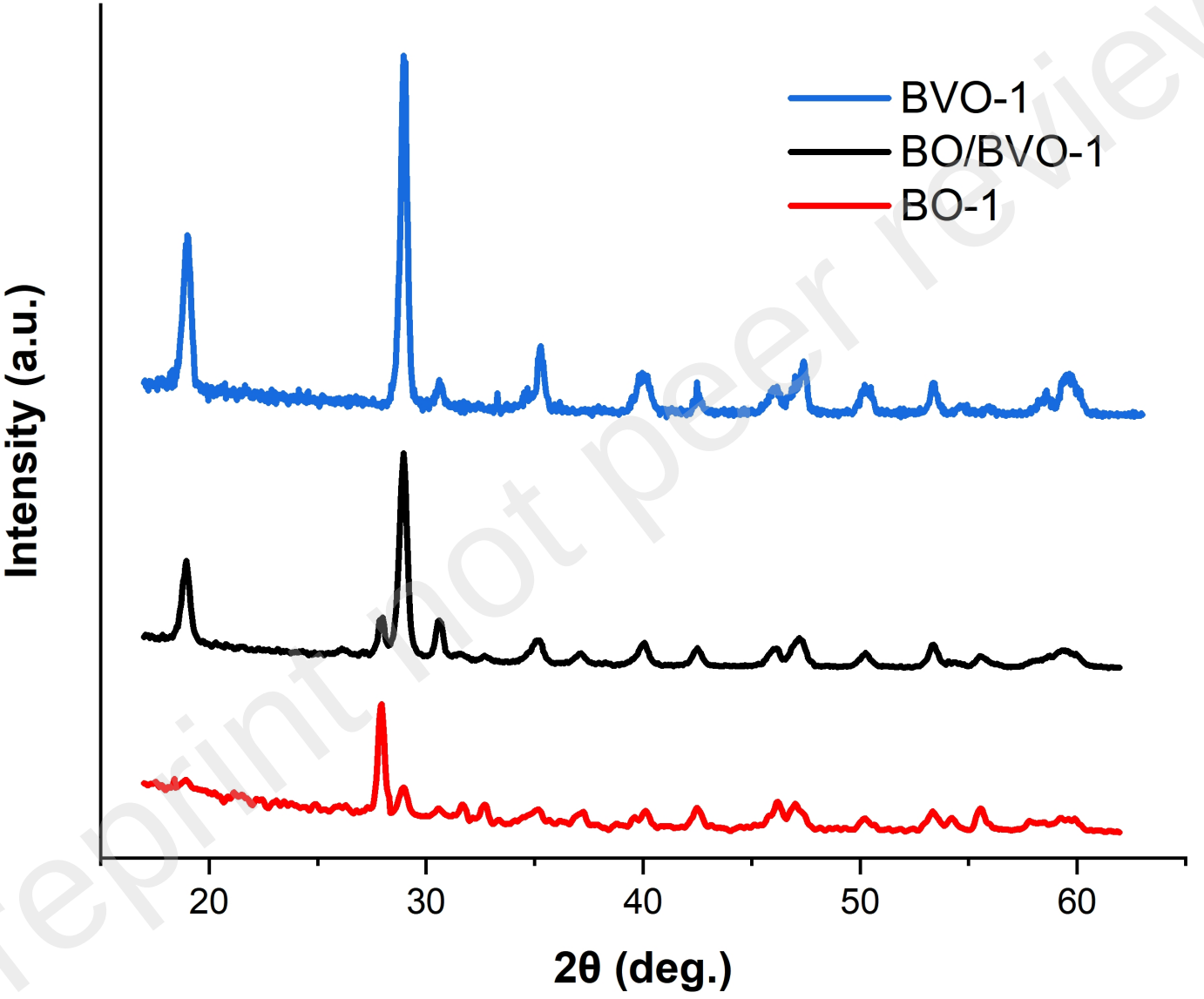

Preprint not peer reviewed

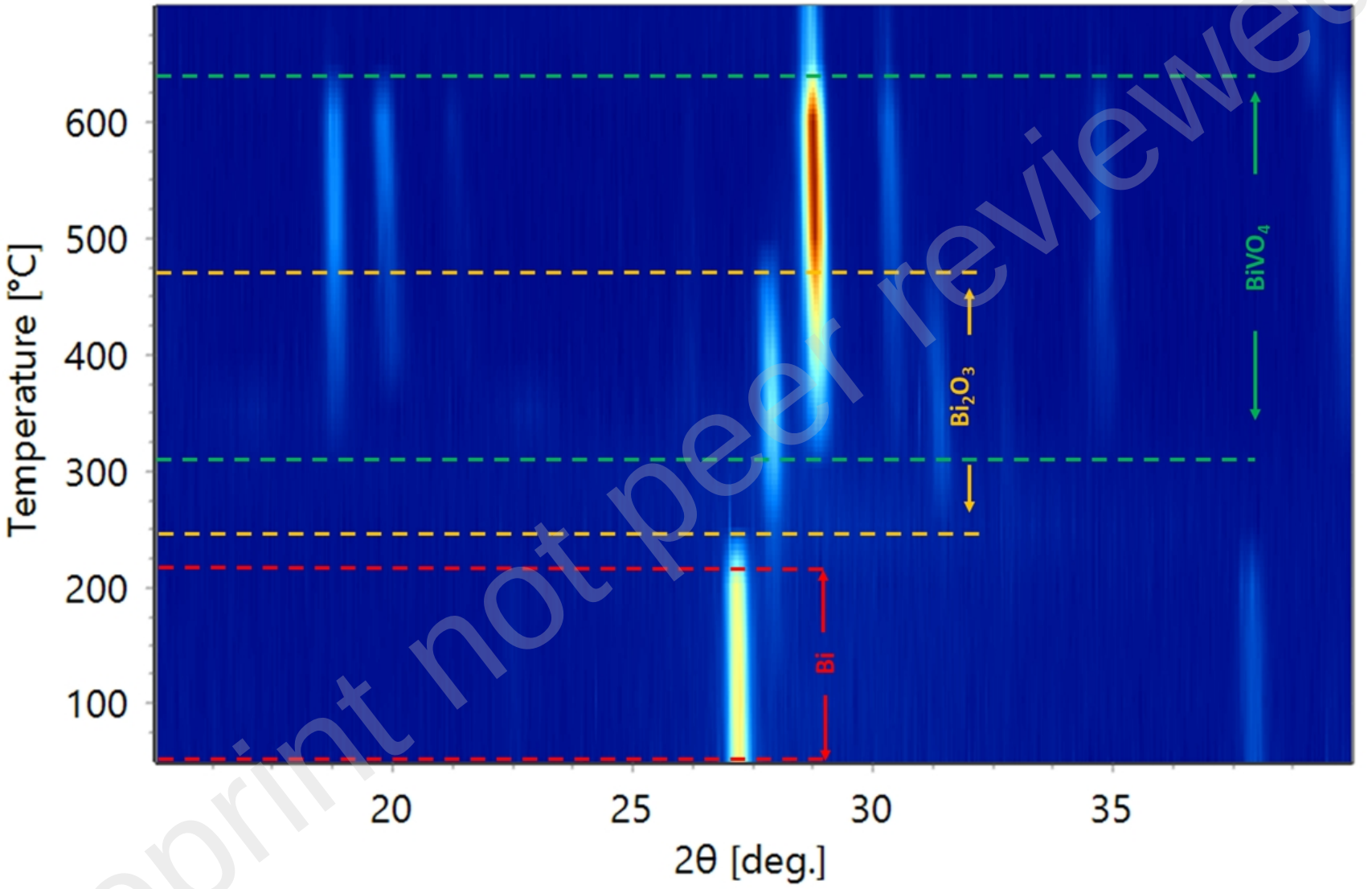

Preprint not peer reviewed

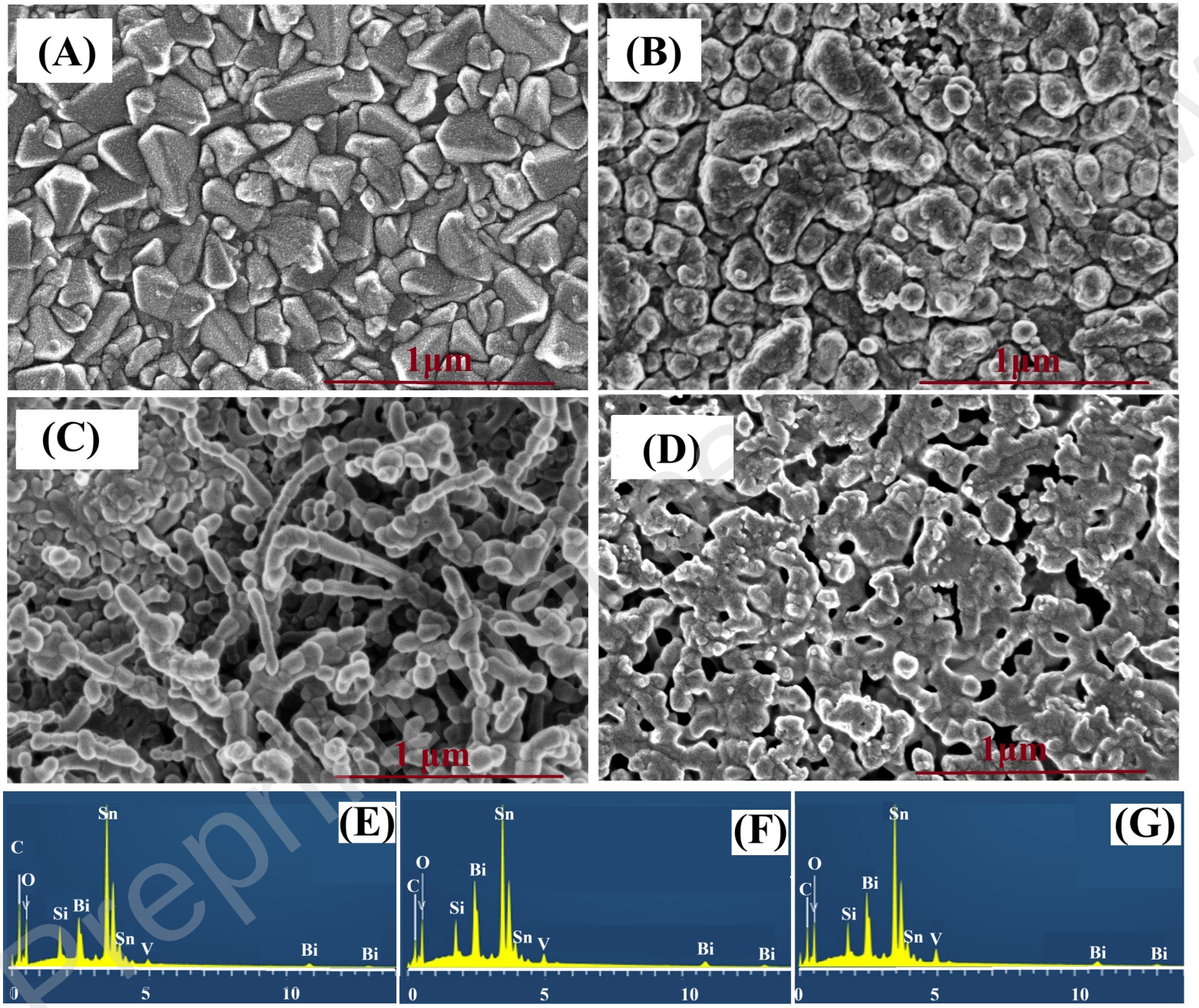
(A)
1μm
(B)
1μm
(C)
1 μm
(D)
1μm
(E)
C
O
Si
Bi
Sn
V
Bi
Bi
0
5
10
(F)
O
C
Si
Bi
Sn
V
Bi
Bi
0
5
10
(G)
O
C
Si
Bi
Sn
V
Bi
Bi
0
5
10

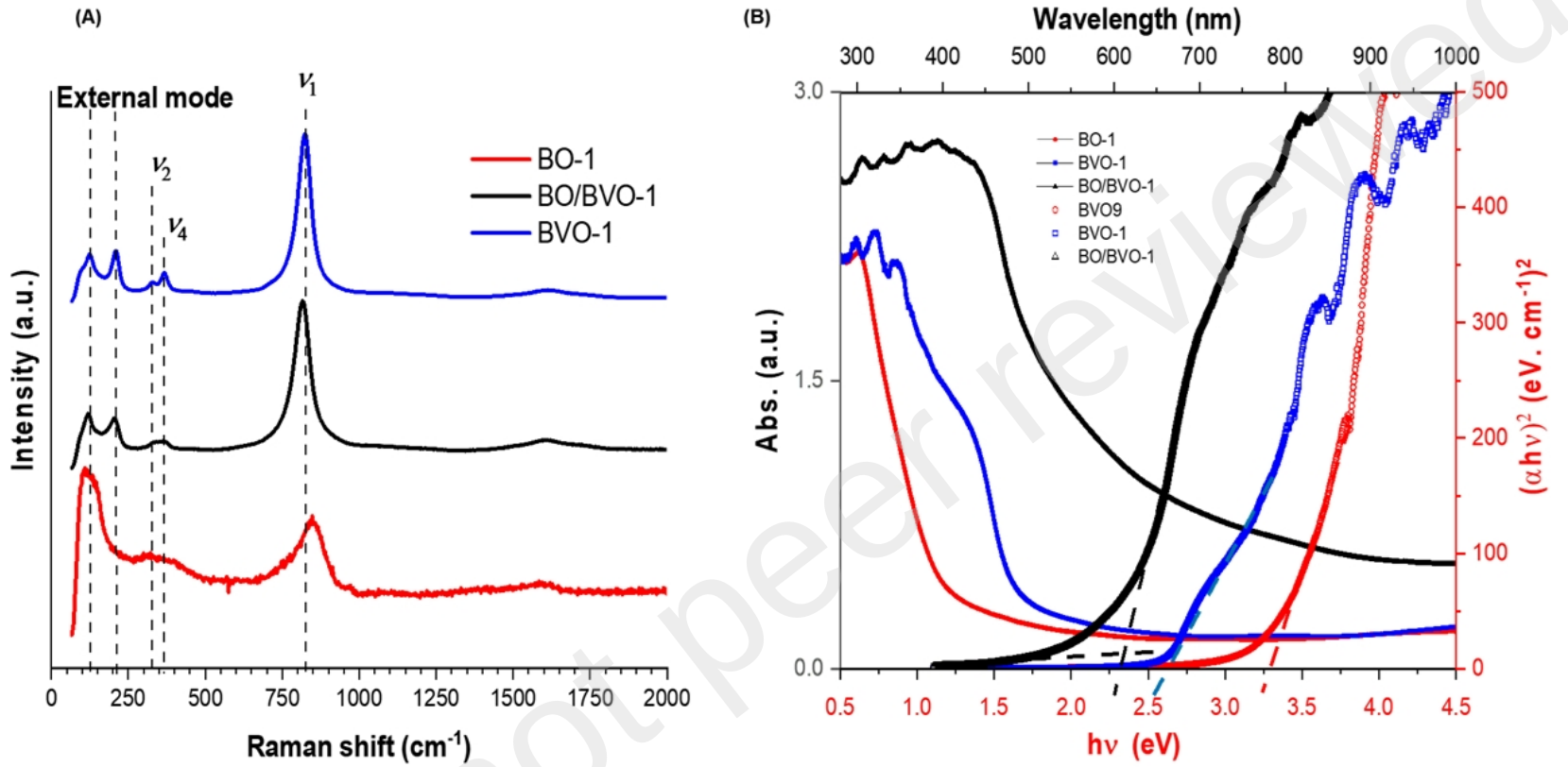

Preprint not peer reviewed

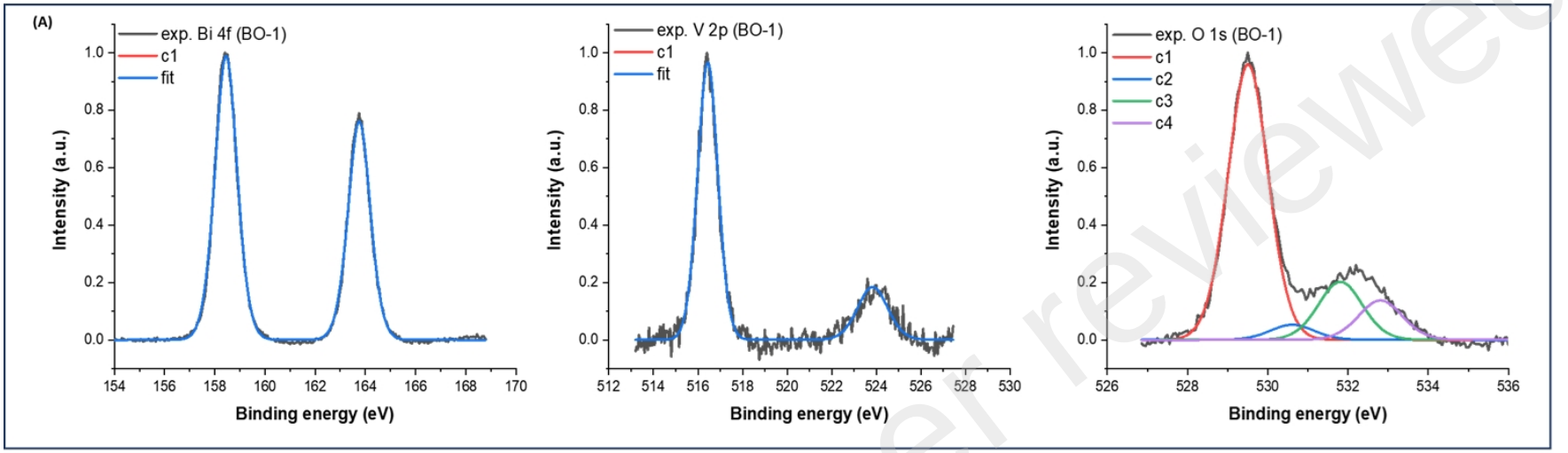

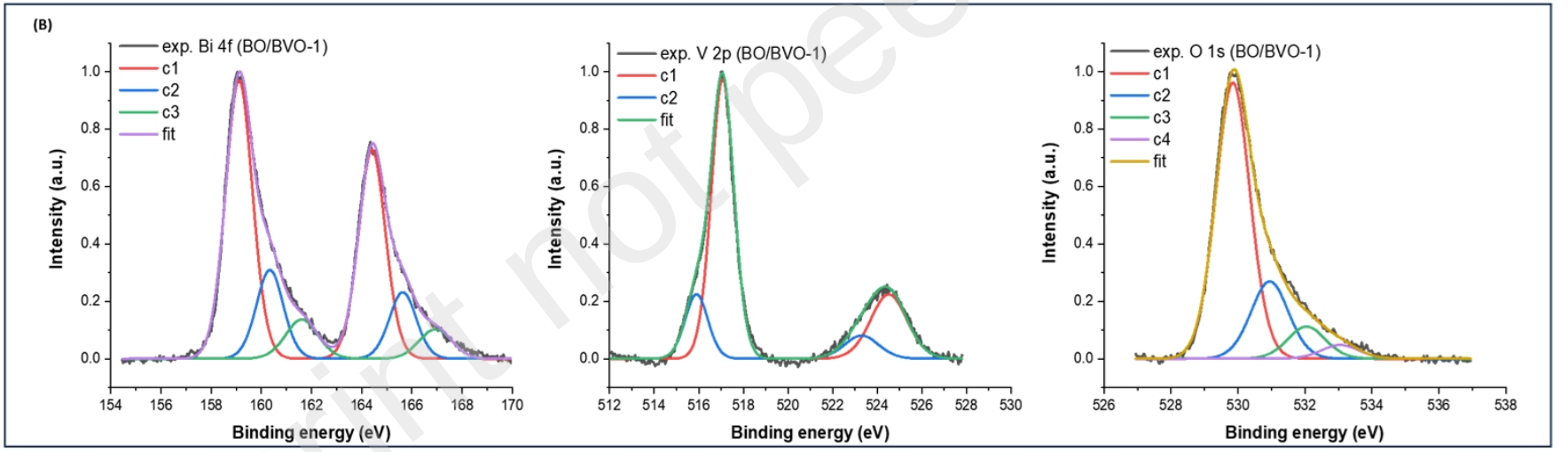

Preprint not peer reviewed

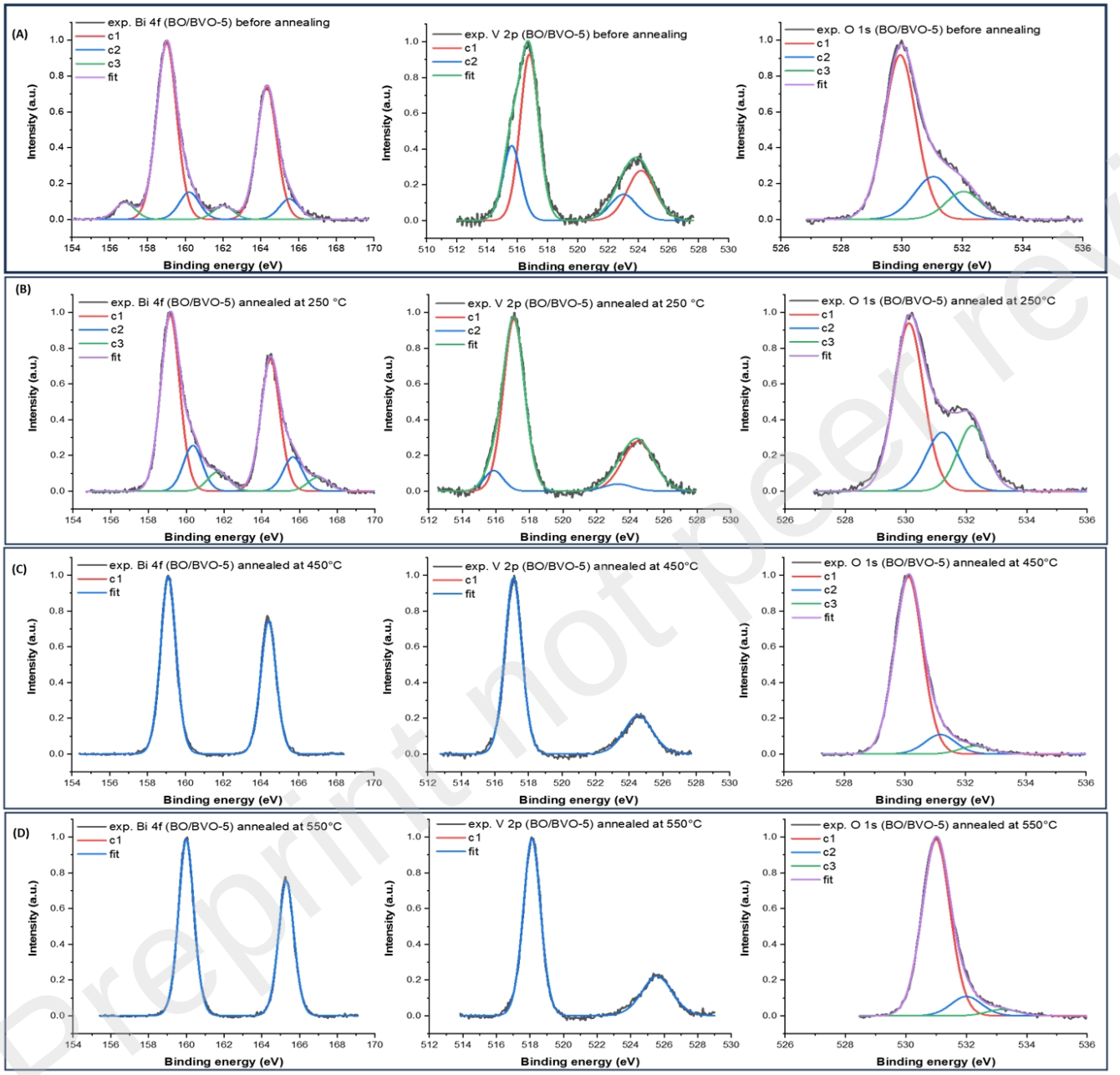

Preprint not peer reviewed

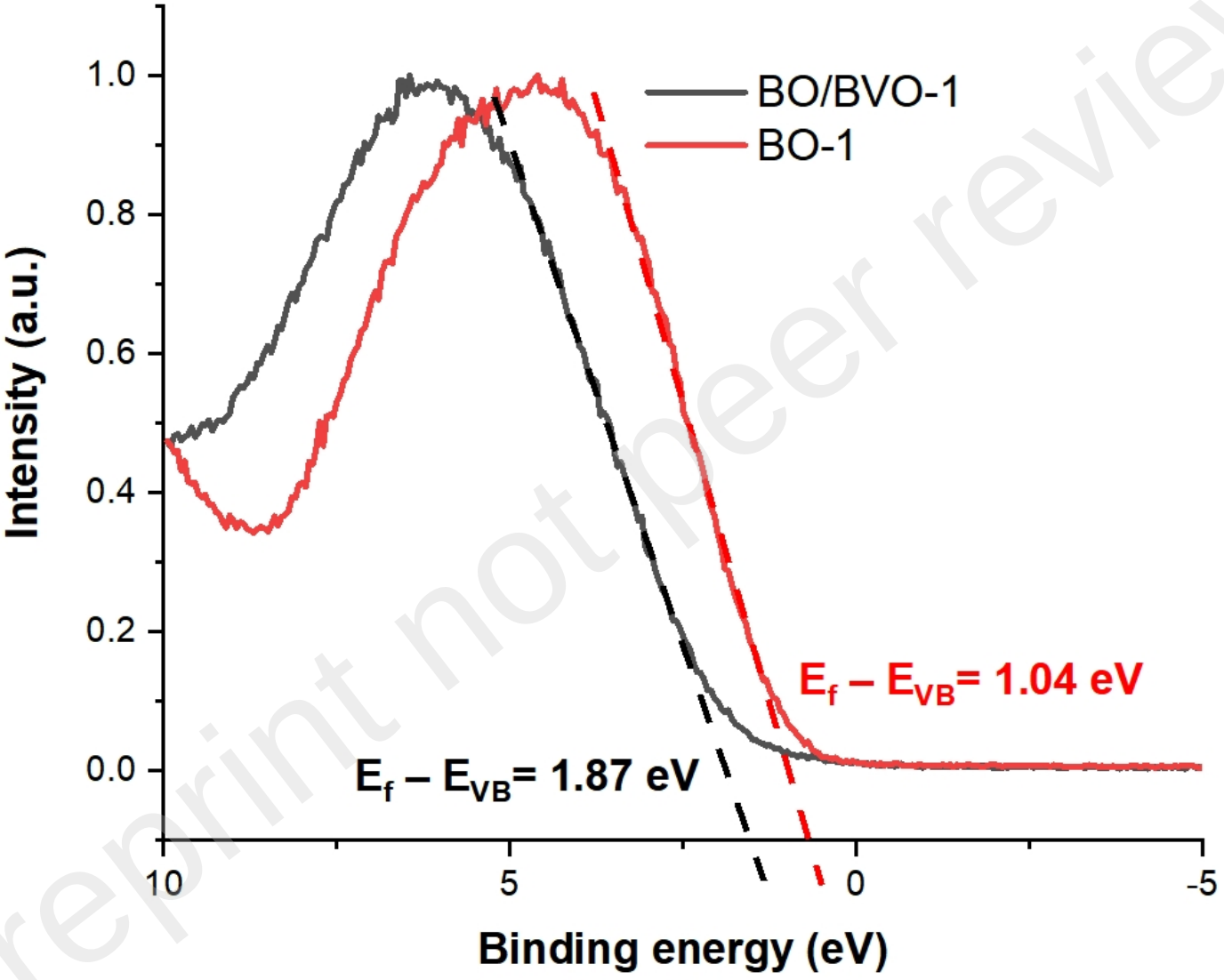

Preprint not peer reviewed

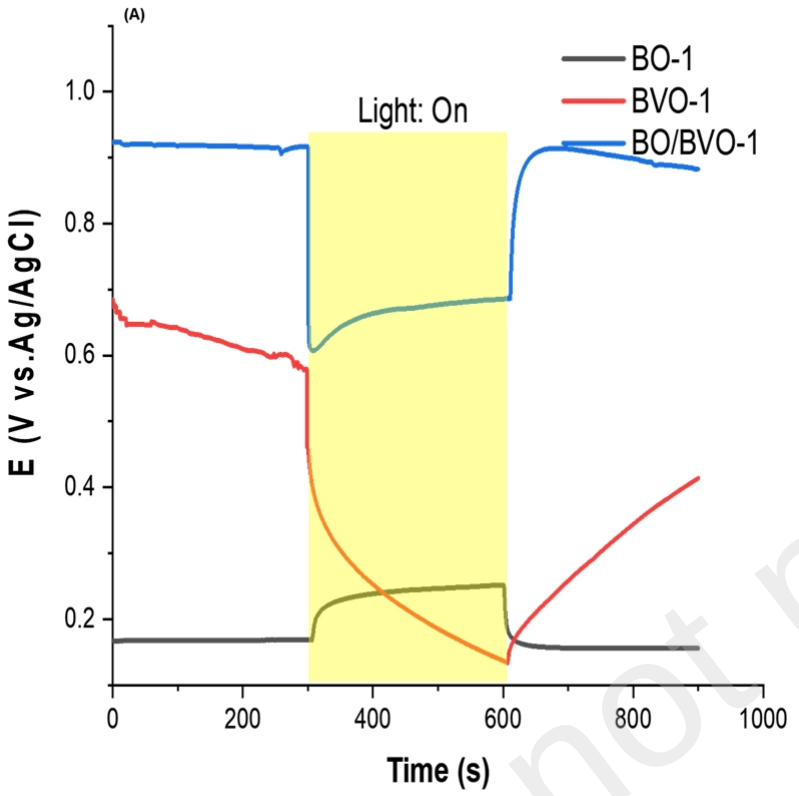

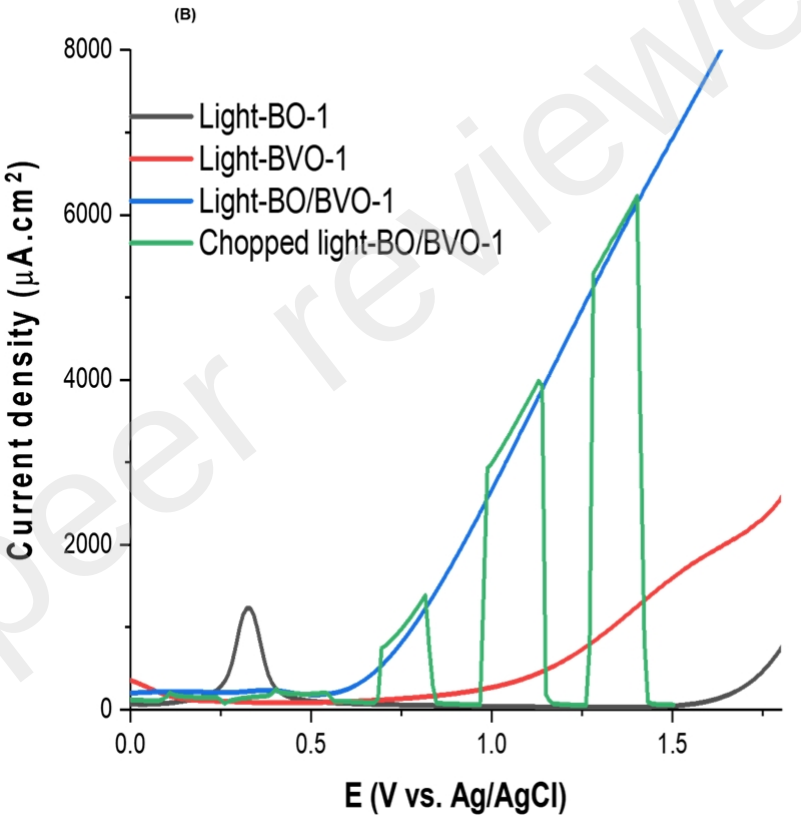

Preprint not peer reviewed

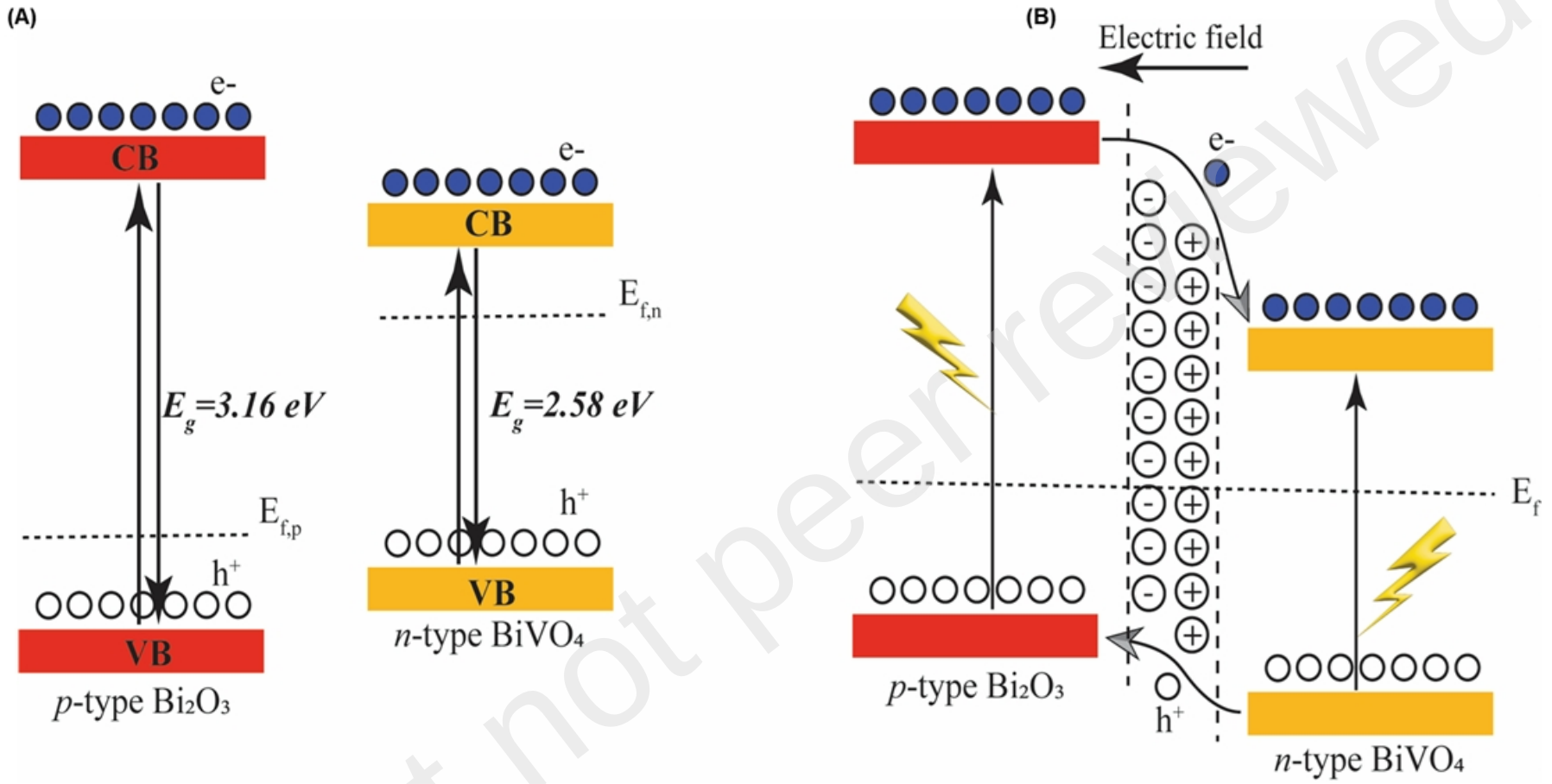

Preprint not peer reviewed

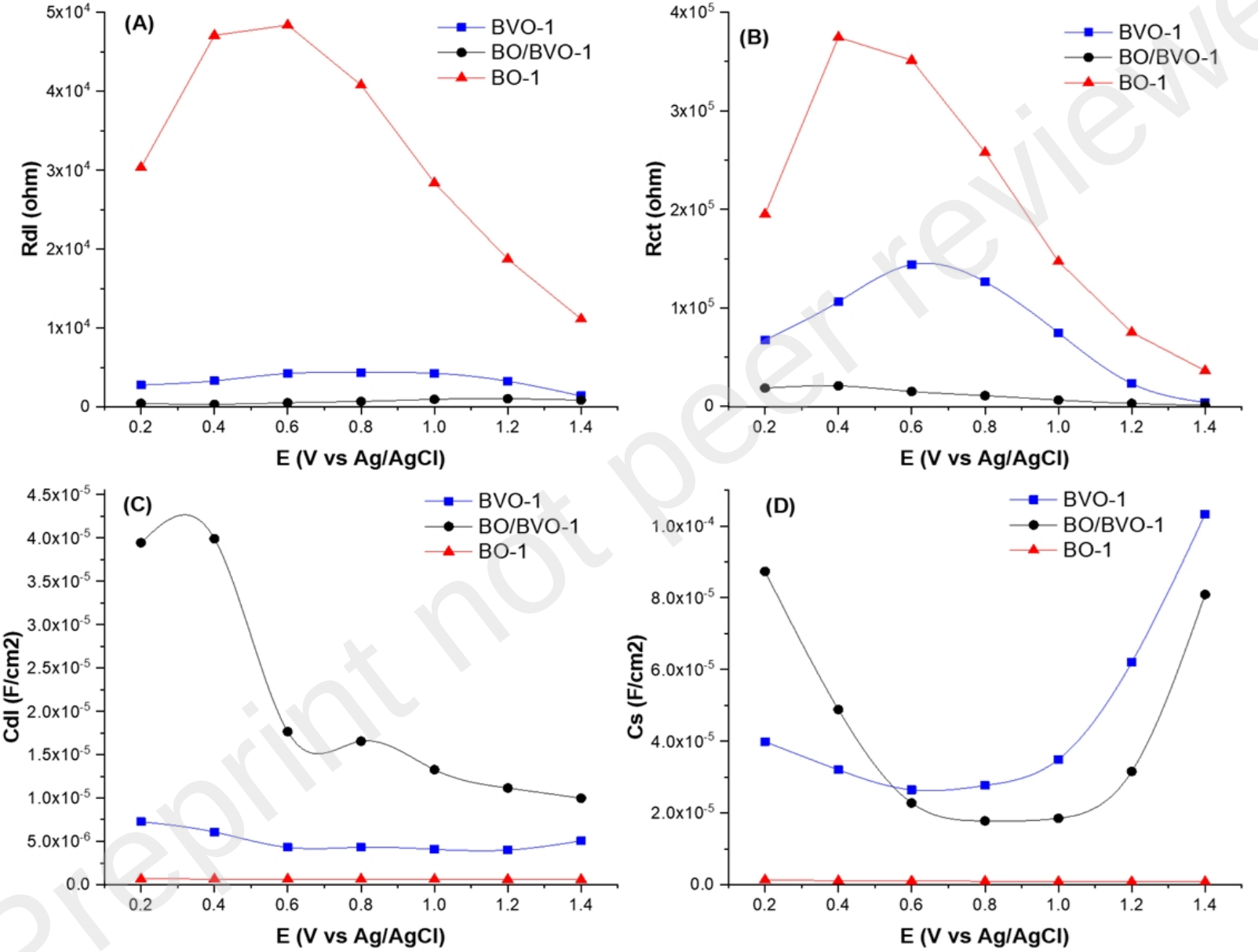

Preprint not peer reviewed